The Thesis Committee for Yining Wang Certifies that this is the approved version of the following Thesis:

Formation of Dense Pyroclasts by Sintering of Ash Particles During the Preclimactic Eruptions of Mt. Pinatubo in 1991

APPROVED BY
SUPERVISING COMMITTEE:

James Gardner, Supervisor

Thomas Giachetti
Jaime Barnes

Formation of Dense Pyroclasts by Sintering of Ash Particles During the Preclimactic Eruptions of Mt. Pinatubo in 1991

by

Yining Wang

Thesis

Presented to the Faculty of the Graduate School of

The University of Texas at Austin

in Partial Fulfillment

of the Requirements

for the Degree of

Master of Science in Geological Sciences

The University of Texas at Austin

May 2019

Acknowledgements

I would like to thank my supervisor Dr. James Gardner for his support and words of wisdom throughout my two years at The University of Texas at Austin. I would also like to thank Dr. Thomas Giachetti and Dr. Jaime Barnes for being on my master's committee and for their kind review and edits. Dr. James Gardner's group members, including Sean O'donnell, Nicholas Meszaros and Nicole Guinn are warmly thanked for their insights and suggestions on my thesis. Lastly, I would like to express my sincere thanks to my family and friends for their unconditional support during my career as a graduate student.

Formation of Dense Pyroclasts by Sintering of Ash Particles During the Preclimactic Eruptions of Mt. Pinatubo in 1991

Abstract

Yining Wang, M.S.GEO.SCI.

The University of Texas at Austin, 2019

Supervisor: James Gardner

Volcanic eruptive behavior varies from explosive tephra or effusive lava and is controlled largely by subsurface degassing processes. Dense cognate lithic pyroclasts are poorly vesicular products of some eruptions. Their textures and dissolved volatile signatures preserve important information about their formation processes and are thus used to infer pre-eruptive and syn-eruptive conduit dynamics. Dense cognate lithics from the 1991 Mt. Pinatubo pre-climactic surge events were analyzed in terms of their vesicular and crystal textures, and dissolved H_2O and CO_2 concentrations. The ubiquitous occurrence of sub-millimeter-sized crystal fragments in matrix glass is an intriguing feature not observed in the pumice counterpart of the Mt. Pinatubo deposits. Existing models of permeable foam behavior cannot explain the fragmentation and reincorporation processes necessary for the formation of these fragments. On the other hand, sub-millimeter scale heterogeneity in matrix-glass volatile content (0.9 wt.% difference in H_2O within 0.5 mm) is observed. Those heterogeneities argue that different parts of these dense pyroclasts must have formed at various depths and then need to be physically sutured together. Greater vesicularities and increased vesicle sizes and number densities are observed around large

crystals and a similar texture was produced by sintering experiments using bimodelly-sized ash particles within a timeframe similar to that of the 1991 Mt. Pinatubo eruptions. Furthermore, an increasingly larger proportion of elongated and stretched vesicles towards the later surge events is observed, which parallels the increasingly shorter hiatus time between Mt. Pinatubo surges. Paired with the lack of equilibration in volatile contents, the textures lead us to propose an ash particle sintering model in deciphering the formation mechanism of these dense lithics in rather short period of time, where ash particles sourced from various depths collide, shear, break up, and sinter on or near the conduit walls above the fragmentation level in a repetitive manner. We conclude that sintering is the main mechanism forming the dense lithic materials from the 1991 Mt. Pinatubo pre-climactic surge deposits, and is responsible for vesicle, crystal, and volatile signatures preserved and observed in this study, and potentially in other volcanic systems around the world.

Table of Contents

List of Tables

List of Figures

Introduction

Volcanic eruptive style, i.e., whether explosive tephra or effusive lava is produced, largely depends on the manner and extent of subsurface degassing (Eichelberger et al., 1986; Hildreth and Drake, 1992; Mastrolorenzo et al., 1993; Mellors and Sparks, 1991; Jaupart and Allegre, 1991; Gonnermann and Manga, 2003). If gas is not physically separated from magma, then degassing happens in a "closed-system", where volatile pressure builds up and causes violent fragmentation. Less violent effusive eruptions are thought to be dominated by "open-system" degassing, in which gas separates from magma through a network of coalesced vesicles. In open-system degassing, the juvenile magma does not disrupt, but instead collapses into a bubble-poor liquid (Eichelberger et al., 1986; Jaupart and Allegre, 1991).

Dense obsidian pyroclasts are commonly observed in eruption products and are used to infer eruptive behavior and degassing processes (Eichelberger and Westrich, 1981; Taylor et al., 1983; Newman et al., 1988; Bursik, 1993; Rust et al., 2004; Gonnermann and Manga, 2005; Rust and Cashman, 2007; Barnes et al., 2014; Gardner et al, 2017). Volatile signatures in obsidian pyroclasts represent closed-system degassing with high H_2O and CO_2 content (Newman et al., 1988; Bursik et al., 1993; Newman et al., 1988; Gonnerman and Manga, 2005; Rust et al., 2004), yet bubbles containing the exsolved gas phase are poorly abundant, which is contrary for closed-system degassing. The poor vesicularity suggests various extents of gas escape, which should only happen in open-system degassing processes. Existing models such as the permeable foam model (Eichelberg et al.,

1986), which suggests that rhyolitic magma vesiculates to form a bubbly foam followed by vesicle coalescence, gas escape, and eventual collapse of the porous network, cannot resolve the discrepancy between observed volatile concentrations and vesicle textures. Other models and hypotheses on the formation of dense obsidian pyroclasts were thus raised, including arguments that the observed closed-system signature originated from disequilibrium bubble growth (Gonnermann and Manga, 2005), from buffering by fluxing vapor (Rust et al., 2004), or from re-equilibration with incorporated xenolith material (Rust and Cashman, 2007). Castro et al. (2014) further proposed a batched degassing model, where pulses of vapor extraction following batched degassing made possible by tuffisite veins are responsible for rapid and explosive gas escape in a closed system which eventually give way to effusive lava.

Recently, Gardner et al. (2017) re-examined the 1325-1350 C.E. North Mono eruption of Mono Craters, CA and observed xenocrystic material between domains of obsidian pyroclasts that may indicate some suturing processes. The differing textures from rounded to distorted vesicles were inferred as reflecting various extent of surface-tension driven relaxation, that is correlated with observed heterogeneities in H_2O and CO_2 concentrations (Gardner et al., 2017). They concluded that the obsidian pyroclasts formed from repeated fragmentation, sintering, and relaxation processes at various depths within the conduit. While sintering serves as a reasonable explanation for formation mechanism of obsidian pyroclasts, whether or not a similar process is responsible for their crystal-rich equivalent - dense cognate lithics that form from juvenile magma, still needs to be examined.

In this study we investigate the textural and volatile data from natural pyroclastic deposits from the 1991 Mt. Pinatubo eruption series in order to understand the conduit dynamics and the formation mechanisms of dense cognate lithics. Hammer et al. (1999)'s study on microlite crystallization during pre-climactic events of the 1991 Mt. Pinatubo provides a timescale in which formation of eruption products and relative timing of clast textures can be framed. Paired with measurements of eruption column heights and well-documented eruptive duration and repose intervals, the 1991 Mt. Pinatubo eruption products serve as an extraordinary suite of natural samples to study the evolution of magmatic processes through eruption series.

Background and Samples

The reawakening of Mt. Pinatubo in 1991 was marked by felt earthquakes and escalating emission of steam and ash starting in March of that year. Volcanic activity is divided and described in seven phases (Table 1) by Hoblitt et al. (1996). The emergence of a lava dome on June 7 provided evidence that the enhanced volcanic activity was driven by rising magma (Hoblitt et al., 1996). The following vertical eruptions in phase IV (Table 1) produced ash clouds that reached heights of >24 km, producing pyroclastic fall deposits extending over a wide area (Hoblitt et al., 1996). The main component of the tephra-fall deposits is andesite scoria, with limited occurrence of dacite (Wolfe and Hoblitt, 1996). The pace of volcanic activity then increased, with thirteen closely-spaced pyroclastic surges becoming the dominant eruption style during June 14-15 (Table 2; Hoblitt et al., 1996), producing progressively more dacitic deposits (Wolfe and Hoblitt, 1996). In general, the intensity of the surge-producing eruptions decreased during this time, but their frequency increased (Table 2). On June 15, 1991, about 5.5 cubic kilometers of pyroclastic-flow and pyroclastic-fall deposits were emplaced during the climactic eruption (Scott et al., 1996). The climactic eruption produced solely dacite, which volumetrically is at least an order of magnitude greater than the deposits produced by the June 12-14 eruptions taken together (Pallister et al., 1996). Overall, the eruptive products contain three major components, classified on whole rock composition: hybrid andesite (59 - 60 wt.% SiO_2), olivine-clinopyroxene basalt (50 – 52 wt% SiO_2), and dacite (64.5 ± 0.3 wt.% SiO_2; Pallister et al., 1996; Luhr and Melson, 1996; Bernard et al., 1996). The pyroclastic dacite is further classified into dense dacite cognate lithics and highly vesicular dacite pumice (with phenocryst-rich and phenocryst-poor endmembers, Hoblitt et al., 1996) based on vesicularity and bulk density.

Phase	Date	Description
I	March 15-May 31	Felt earthquakes; emission of steam and minor ash; release of seismic energy
II	June 1-June 7	Escalating seismic-energy release; diminution in SO_2 emission; inflationary tilt
III	June 7-June 12	Growth of lava dome; increasing emission of ash and seismic-energy release
IV	June 12-June 14	4 vertical eruptions; minor pyroclastic flows; continued dome growth
V	June 14-June 15	Multiple surge-producing eruptions
VI	June 15	Climactic eruption (large vertical eruption and pyroclastic flows);
VII	June 15-early September	Continued ash emission and intermittent small ash eruptions

Table 1: Chronology of the 1991 Pinatubo eruptions (Hoblitt et al., 1996).

In this study, we focus on textural and volatile analyses of dense dacite lithics from the pre-climactic surge events (Phase V). The sample suite consists of 48 dacite lithic clasts (Table 2) that are 2 – 10 mm in size from pyroclastic surge deposits collected in March 1992, from site #11 (Hoblitt et al., 1996), the most proximal site to the southeast of the caldera. Only 11 out of the 13 pre-climactic surges are thought to be present at site #11, and among those, 9 surge deposits yielded sufficient deposit to be sampled and analyzed (Table 2). In addition, a dacite pumice sample (P351) from surge 3 is studied, as a comparison in terms of vesicle and matrix glass texture.

Date	surge event	repose since previous event (min)	seismic duration (min)	plume ht (km)	n. dacite lithic samples
6/14/91	1	124	7		7
6/14/91	2	210	5	≥24	0
6/14/91	3	262	3	21	8 (+ 2 dacite pumice)
6/15/91	4	112	3-23	?	4
6/15/91	5	79-99	4	?	4
6/15/91	6	174	3	12	1
6/15/91	7	132	?	12?	2
6/15/91	8	137	4-14	15?	5
6/15/91	9	36-46	4-13	?	12 (+ 1 dacite pumice)
6/15/91	10	28-37	9	8	5
6/15/91	11	15	10	?	0
6/15/91	12	20	4	?	0
6/15/91	13	19	13	?	0

Table 2: 1991 Mt. Pinatubo eruption chronology for Phase V (data from Hoblitt et al., 1996) and number of samples.

Methods

Samples larger than 8 mm in diameter were broken into pieces with a steel mortar and pestle. A select number of pieces were mounted in epoxy and polished on both sides for optical microscopy analysis and scanning electron microscopy. The resulting cross-sectional area polished for microscopy analysis range from 6.4 mm^2 to 31.2 mm^2. Thin sections of pyroclastic clasts were thinned until sufficient light could pass through the glass to facilitate avoiding phenocrysts and clusters of vesicles, microlites, and crystal fragments for matrix glass volatile measurement. Thin wafers were doubly-polished to a thickness between 50 μm to 160 μm.

TEXTURAL ANALYSIS

The textures of the dense cognate lithics were studied using a combination of Scanning Electron Microscopy (SEM) and optical microscopy. First, a subset of 44 out of the 48 samples were polished and scanned using a Phillips/FEI XL30 Environmental Scanning Electron Microscope (The University of Texas at Austin) to produce Back-Scattered Electrons (BSE) images and compositional x-ray maps. The BSE images were used to measure vesicularity, which is defined as the area of void space divided by the total area of void space and matrix glass. For crystal abundance, stacked X-ray maps of Fe, Mg, Ca, Na, Al, P, Ti, S were used for mineral identification, as these elements cover almost all the mineral phases in the samples, except quartz, which was selected manually with the Si X-ray maps. Crystallinity can thus be calculated, which is defined as total area of crystals divided by total area of clast excluding all voids. Matrix glass abundance was calculated by subtracting total area by void area and crystal area. All image analyses were done using *AZtec* and *ImageJ*. On each whole clast BSE images, small sub-domains sized from 0.024 mm^2 to 0.68 mm^2 with various vesicularity were selected randomly and further measured

in terms of vesicularity and were later studied using an optical microscope, to measure vesicle sizes, shapes and 3D vesicle number densities.

Vesicle sizes, number densities, and spatial distribution were studied using optical microscopy. Vesicles in transparent glass matrix were counted within rectangular columns in the selected sub-domains as we focused through samples at magnification of 500X. All vesicles in columns were counted and measured until individual vesicles could no longer be identified. The thickness traveled through the sample was recorded by a linear drive encoder attached to the focusing drive of the microscope. All identifiable vesicles in columns are measured in terms of long and short axes using the eyepiece reticle with a precision of 1 μm. A dimensionless bubble deformation parameter is calculated, which is defined as (Taylor, 1934; Rust and Manga, 2002):

$$D = \frac{l_a - l_b}{l_a + l_b} \quad (1)$$

Where l_a and l_b are the long and short axes of vesicles. For vesicles with long and short axes ambiguous or hard to define, for distorted vesicles particularly, the longest and shortest spans of vesicles were measured to determine *D*.

GLASS COMPOSITION

A total of 60 spots on matrix glass were analyzed (Table 3; Table 11, appendix) using a JEOL JXA-8200 Electron Microprobe (EPMA) at the University of Texas at Austin. One clast from each of the surges 1, 3, 4, 5, 6, 8, 9, and 10 were analyzed and six to eleven spots were measured in each while avoiding microlites, crystal fragments, and vesicles. An accelerating voltage of 15 kV, a beam current of 10 nA, and a defocused spot size of 10 μm were used to minimize Na migration. Automatic drift corrections were used on standard intensities, with working standards analyzed repetitively to monitor instrumental drift. Because of the presence of volatiles, dissolved H_2O in particular, the

sums of major elements do not sum to 100 wt.%. The concentrations of major oxides were thus normalized so that their totals equal to 100 wt.%.

sample	surge event	n. of measurements	SiO_2 (wt.%)	TiO_2 (wt.%)	Al_2O_3 (wt.%)	FeO (wt.%)	MnO (wt.%)	MgO (wt.%)	CaO (wt.%)	Na_2O (wt.%)	K_2O (wt.%)	normalized sum (wt.%)
1-1B	1	6	78.17 (0.42)	0.12 (0.03)	12.36 (0.14)	0.84 (0.09)	0.03 (0.01)	0.22 (0.08)	1.11 (0.11)	4.04 (0.18)	3.13 (0.06)	100
1-2B	3	7	78.77 (0.21)	0.15 (0.05)	12.15 (0.19)	0.84 (0.14)	0.04 (0.02)	0.17 (0.03)	1.02 (0.05)	3.61 (0.15)	3.25 (0.03)	100
1-3B	4	11	78.66 (0.24)	0.13 (0.03)	12.40 (0.16)	0.75 (0.06)	0.03 (0.02)	0.18 (0.04)	1.04 (0.06)	3.65 (0.22)	3.16 (0.12)	100
1-4B	5	8	78.37 (0.17)	0.12 (0.04)	12.55 (0.13)	0.73 (0.05)	0.03 (0.03)	0.18 (0.03)	1.05 (0.03)	3.88 (0.09)	3.09 (0.08)	100
1-5A	6	6	77.96 (0.62)	0.13 (0.03)	12.78 (0.42)	0.71 (0.04)	0.05 (0.03)	0.11 (0.03)	1.19 (0.10)	4.05 (0.20)	3.03 (0.16)	100
1-8C	8	8	78.08 (0.26)	0.15 (0.02)	12.57 (0.08)	0.82 (0.09)	0.03 (0.03)	0.19 (0.02)	1.08 (0.04)	4.00 (0.13)	3.08 (0.07)	100
1-9D	9	7	77.76 (0.28)	0.12 (0.02)	12.72 (0.10)	0.78 (0.07)	0.03 (0.03)	0.22 (0.05)	1.15 (0.03)	4.12 (0.22)	3.10 (0.05)	100
1-10B	10	7	77.81 (0.38)	0.11 (0.03)	12.65 (0.19)	0.80 (0.04)	0.04 (0.02)	0.23 (0.03)	1.19 (0.06)	4.04 (0.17)	3.13 (0.08)	100

Values are surge averages. () = 1σ.

Table 3: Sample average oxide concentrations measured in matrix glass in dacite lithics from the 1991 Mt. Pinatubo surge deposits.

VOLATILE MEASUREMENTS

A total of 329 spots were analyzed using Fourier transform infrared spectroscopy (FTIR) in 34 obsidian pyroclasts for dissolved H_2O content. In addition, 275 of those also yielded measurements for CO_2 contents. The data cover a range of eight stratigraphic units of surge deposits from the preclimactic eruption series. Spectra were obtained for the range of 7800 to 4000 cm^{-1} using 120 scans, a liquid-nitrogen-cooled detector, white light, and KBr beamsplitter. The aperture size was fixed to a square of 50 × 50 μm. We attempted to measure at least 10 spots in each pyroclast, so that measurements span various textures. Absorbances at wavenumbers of 5200 cm^{-1} (hydroxyl (OH)) and 4500 cm^{-1} (molecular H_2O) are used to calculate dissolved H_2O contents using the model of Zhang et al. (1997).

Absorbance at 2350 cm^{-1} was used to calculate CO_2 content. When CO_2 spectra displayed negative peaks on both sides of the positive peak, two extreme values were taken (maximum CO_2 content with base defined by the bottom of negative peaks; minimum CO_2 content with base defined by the top of the negative peaks). The two extreme values were then averaged to determine CO_2 concentrations. The CO_2 measurement is not made whenever a positive peak is absent.

DACITE PUMICE

Three pumice samples are analyzed in comparison to dense cognate lithics in terms of vesicle and crystal textures. P351 is the same sample used by Hammer et al. (1999). The sample is mounted in epoxy and polished on one side to a thickness ~30 μm for microscopy studies. Vesicularity and mineralogy of crystal phases are analyzed using an optical microscope. Two other pumice clasts (from surge 3 and surge 9) were scanned using the High-Resolution X-ray Computed Tomography Facility at the University of Texas at 160 kV, 0.2 mA, with a voxel size of 9.6 μm. 16bit TIFF images were produced from each scan and were used to conduct image analyses.

Results

VESICLE SHAPE

Three clasts contained no vesicles (Table 4). Vesicle shapes in a subset of 36 out of all 48 dense cognate lithic samples are classified following a classification scheme (Figure 1) expanded from that of Gardner et al. (2017). All vesicles are classified into two main shapes: regular or irregular. Regularly shaped vesicles with a *D* between 0 and an arbitrary threshold of 0.1 are classified as spherical vesicles. If they have smooth surfaces, they are then named "smooth spherical" (Figure 2A, B), as opposed to "rough spherical" (Figure 2C) vesicles with rough contourted surfaces. Regularly shaped vesicles with a *D* greater than 0.1 are ellipzoidal. Among those, some ellipzoidal vesicles have smooth surfaces (Figure 2B), rough surfaces (Figure 2C), or sharp tip(s) on one or both ends of the long axes (Figure 2E-H). Irregularly shaped vesicles bear no symmetry and are not in a general form of sphere or ellipzoid. These vesicles are classified as either "stretched distorted" (Figure 2D), if they are distorted yet stretched in certain direction, or "distorted" (Figure 2E).

Table 4 Vesicle texture and dissolved volatile concentrations in the 1991 Mt. Pinatubo pre-climactic dense cognate lithics.

sample	surge event	repose since previous event (min)	no. vesicles measured	avg. length (μm)	avg. width (μm)	D[1]	n. prisms measured	avg. vesicle number density (vesicles / mm^3)	whole clast vesicularity (%)	whole clast crystalinity (%)	n. analyses (H_2O)	avg. H_2O (wt.%)	n. analyses (CO_2)	avg. CO_2 (ppm)
3-6A	1	124	107	6.25 (4.94)	3.95 (2.57)	0.23	16	318910 (148042)	29.67	47.68	0	n.d.	0	n.d.
3-6B	1	124	90	14.07 (9.37)	10.16 (7.58)	0.16	20	74502 (51689)	34.21	52.70	0	n.d.	0	n.d.
3-6C	1	124	79	5.30 (2.02)	4.12 (1.78)	0.12	11	388034 (199100)	6.77	55.21	0	n.d.	0	n.d.
3-6D	1	124	n.d.	n.d.	n.d.	n.d.	n.d.	n.d.	n.d.	n.d.	9	1.30 (0.15)	3	9 (2)
3-6E	1	124	98	9.79 (6.23)	7.27 (4.00)	0.15	16	169976 (98372)	24.35	53.67	0	n.d.	0	n.d.
1-1A	1	124	no vesicles	n.d.	n.d.	n.d.	n.d.	n.d.	14.31	53.17	0	n.d.	0	n.d.
1-1C	1	124	n.d.	n.d.	n.d.	n.d.	n.d.	n.d.	13.80	40.95		n.d.		n.d.
1-2A	3	262	120	9.90 (6.38)	7.20 (4.50)	0.16	49	154986 (313799)	27.71	51.31	10	1.88 (0.21)	10	25 (5)
1-2B	3	262	88	8.70 (4.97)	6.77 (3.51)	0.12	15	225752 (110561)	12.89	42.88	10	1.28 (0.22)	10	18 (6)
1-2C	3	262	89	6.25 (2.29)	4.96 (1.83)	0.12	13	444827 (230551)	5.72	53.69	10	1.83 (0.18)	10	28 (3)
1-2L-A	3	262	110	9.08 (4.09)	6.88 (3.08)	0.14	18	304495 (161431)	28.71	50.97	10	1.62 (0.14)	10	22 (4)
1-2L-B	3	262	45	8.91 (3.92)	6.71 (2.63)	0.14	10	163115 (131719)	10.89	51.43	10	1.30 (0.43)	10	19 (5)
1-2L-C	3	262	108	9.63 (6.40)	7.65 (5.33)	0.11	20	162620 (113783)	12.63	46.23	13	1.55 (0.22)	13	22 (3)
1-2L-D	3	262	95	9.01 (5.17)	7.23 (4.40)	0.11	20	156612 (119365)	8.88	46.43	0	n.d.	0	n.d.
1-2L-E	3	262	135	8.90 (5.17)	7.19 (3.91)	0.11	23	192977 (97136)	9.93	44.02	10	1.65 (0.25)	10	21 (5)
1-3A	4	112	102	6.81 (3.82)	5.40 (3.19)	0.12	20	302882 (94130)	8.30	47.65	10	1.79 (0.23)	9	18 (4)
1-3B	4	112	53	10.87 (5.73)	8.70 (4.32)	0.11	10	97849 (54476)	4.17	47.41	10	1.72 (0.13)	10	15 (4)
1-3C	4	112	29	7.59 (4.00)	5.79 (2.72)	0.13	8	266963 (197872)	21.13	57.55	4	1.64 (0.06)	4	21 (5)
1-3D	4	112	43	9.95 (4.27)	7.51 (4.27)	0.14	9	142071 (72246)	6.72	52.53	11	1.98 (0.27)	11	18 (4)
1-4A	5	90	no vesicles	n.d.	n.d.	n.d.	n.d.	n.d.	7.69	46.96		n.d.		n.d.
1-4B	5	90	no vesicles	n.d.	n.d.	n.d.	n.d.	n.d.	n.d.	53.67	10	1.63 (0.19)	10	15 (4)
1-4C	5	90	59	8.58 (3.47)	7.07 (3.22)	0.10	11	162446 (66029)	13.51	60.15	10	1.87 (0.10)	10	15 (3)
1-4D	5	90	44	12.30 (5.29)	9.27 (4.27)	0.14	9	94778 (42645)	13.91	46.25	10	1.96 (0.14)	10	20 (4)
1-5A	6	174	46	5.09 (2.69)	4.17 (2.18)	0.10	14	485160 (234714)	8.67	48.43	10	1.55 (0.26)	10	20 (4)
1-6A	7	132	n.d.	n.d.	n.d.	n.d.	n.d.	n.d.	43.69	51.94		n.d.		n.d.
1-6D	7	132	n.d.	n.d.	n.d.	n.d.	n.d.	n.d.	44.76	37.02		n.d.		n.d.
1-8A	7	137	99	18.47 (6.74)	15.99 (5.40)	0.07	23	14686 (8461)	20.29	48.82		n.d.		n.d.
1-8B	8	137	19	10.89 (4.75)	8.32 (3.51)	0.13	4	132197 (39558)	7.80	53.97	10	1.67 (0.33)	10	23 (4)
1-8C	8	137	n.d.	n.d.	n.d.	n.d.	n.d.	n.d.	9.46	52.49	10	1.65 (0.22)	10	10 (3)
1-8D	8	137	n.d.	n.d.	n.d.	n.d.	n.d.	n.d.	32.68	50.41	4	1.81 (0.04)	4	19 (1)
1-8E	8	137	n.d.	n.d.	n.d.	n.d.	n.d.	n.d.	11.26	47.28	8	1.38 (0.20)	7	8 (3)
1-9B	9	46	94	15.64 (6.59)	10.56 (5.07)	0.19	23	80482 (35812)	24.28	47.31	2	1.08 (0.08)		n.d.
1-9C	9	46	118	12.93 (6.83)	9.64 (5.51)	0.15	23	133349 (55060)	9.35	55.71	10	1.29 (0.15)	10	10 (2)

1-9D	9	46	117	12.75 (6.73)	9.49 (5.07)	0.15	22	103711 (55526)	4.44	58.75	10	1.57 (0.51)	7	9 (1)
1-9E	9	46	88	9.14 (4.61)	7.24 (3.83)	0.12	19	187070 (133917)	7.71	51.23	11	1.79 (0.29)	1	11
1-9L-A	9	46	60	11.58 (6.28)	8.00 (3.49)	0.18	16	127763 (63392)	n.d.	n.d.	10	1.48 (0.20)	11	8 (2)
1-9L-B (Pt 1)	9	46	111	8.49 (5.03)	7.48 (3.66)	0.06	25	143700 (55369)	8.32	47.05	10	1.45 (0.11)	9	16 (3)
1-9L-B (Pt 2)	9	46	124	9.70 (4.03)	7.14 (8.53)	0.15	20	160469 (70161)	12.50	46.38	0	n.d.	0	n.d.
1-9L-C (Pt 1)	9	46	119	12.36 (7.93)	8.78 (5.14)	0.17	21	63591 (23990)	12.24	49.70	9	1.44 (0.19)	6	5 (1)
1-9L-C (Pt 2)											10	1.53 (0.35)	4	9 (2)
1-9L-D	9	46	106	14.24 (8.15)	10.63 (6.68)	0.14	26	88359 (45722)	37.08	50.21	9	1.31 (0.23)	6	9 (1)
1-9L-E	9	46	71	22.73 (9.97)	16.90 (8.22)	0.15	20	58996 (38907)	79.91	69.95	0	n.d.	0	n.d.
1-9L-F	9	46	n.d.	n.d.	n.d.	n.d.	n.d.	n.d.	41.74	49.89	0	n.d.	0	n.d.
1-10A	10	33	135	6.25 (4.58)	3.84 (2.04)	0.24	14	455461 (144965)	12.18	43.44	10	1.36 (0.22)	3	7 (1)
1-10B	10	33	104	11.28 (4.68)	9.04 (3.78)	0.11	17	77094 (38820)	11.85	46.27	10	1.134 (0.32)	10	7 (1)
1-10C	10	33	100	5.19 (4.08)	2.73 (1.25)	0.31	13	167897 (151139)	17.68	49.37	11	1.30 (0.08)	8	5 (1)
1-10D	10	33	149	6.52 (4.17)	4.40 (5.91)	0.19	18	373690 (110657)	5.73	43.13	10	1.60 (0.21)	7	8 (1)
1-10E	10	33	202	6.29 (5.12)	3.88 (2.07)	0.24	23	455219 (158244)	13.62	55.11	12	1.58 (0.26)	4	6 (1)

Values are clast averages. () = 1σ. N.d. = not determined
[1] calculated from clast average length and average width

Table 4: Vesicle texture and dissolved volatile concentrations in the 1991 Mt. Pinatubo pre-climactic dense cognate lithics.

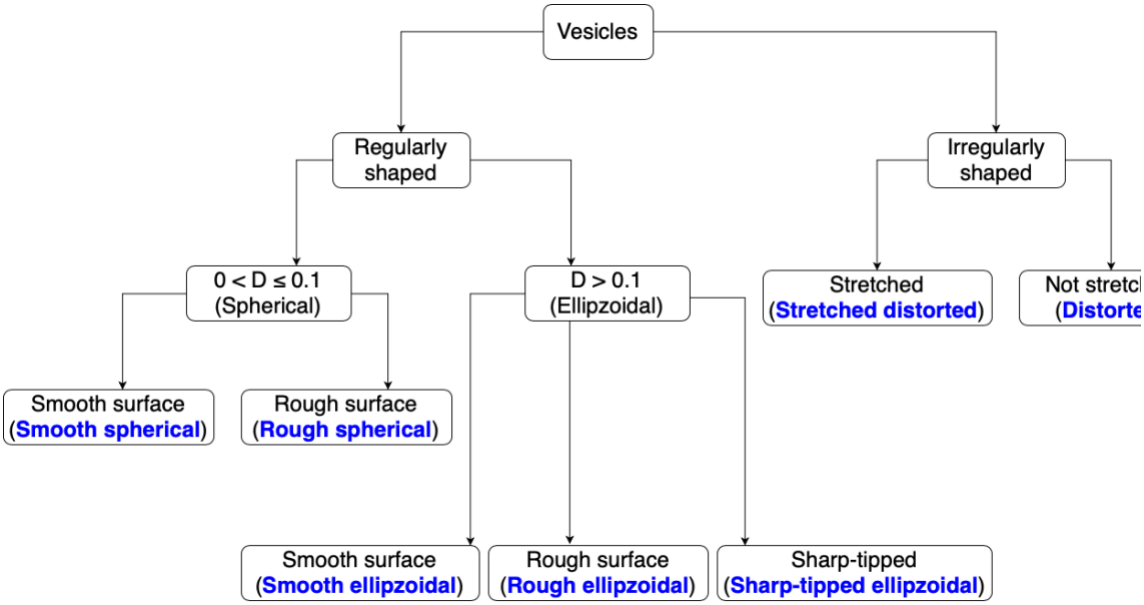

Figure 1: Vesicle classification flow chart.

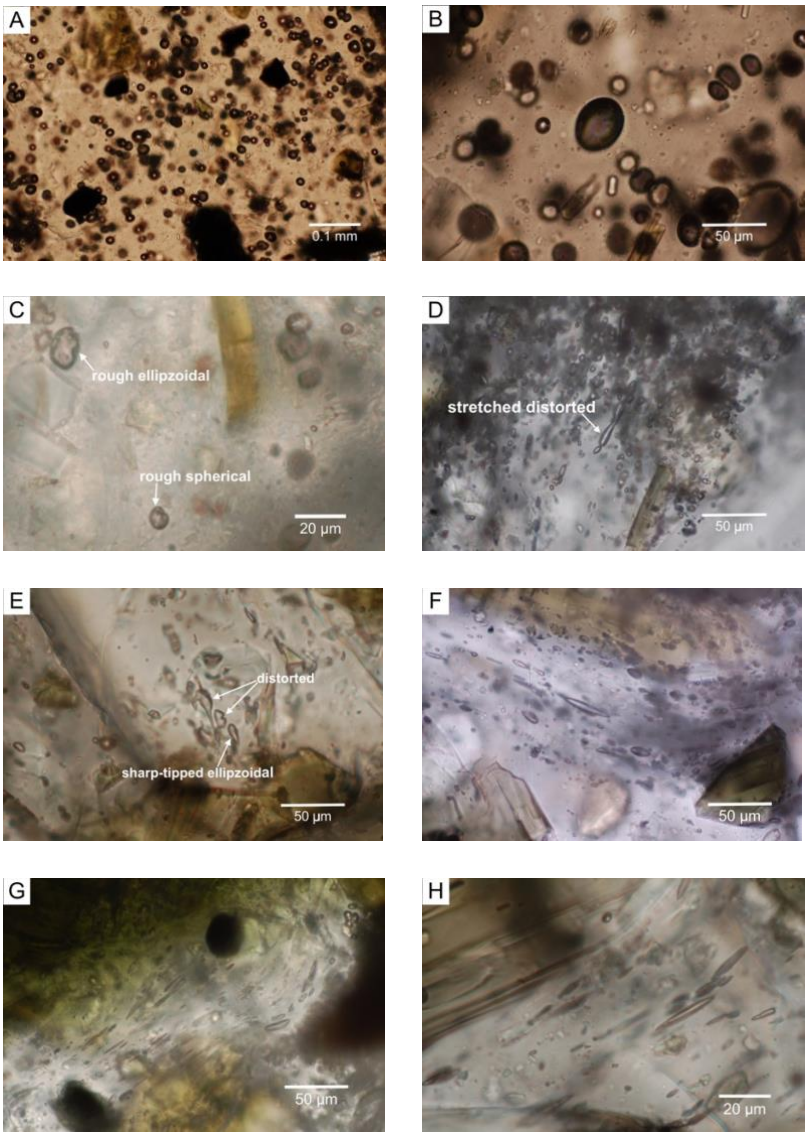

Figure 2: Optical microscope images showing vesicles shapes observed in polished thin sections made from 1991 Mt. Pinatubo surge deposits. **A** Homogeneously distributed smooth spherical vesicles in sample 1-8A (surge 8). **B** Smooth ellipzoidal and smooth spherical vesicles in sample 1-8A (surge 8). **C** Rough ellipzoidal and rough spherical vesicles in sample 1-2L-C (surge 3). **D** Stretched distorted vesicle in a context with various degrees of vesicle relaxation in sample 1-10A (surge 10) **E** Sharp-tipped ellipzoidal and distorted vesicles in sample 1-10A (surge 10). **F-H** Sharp-tipped ellipzoidal vesicles in flow-bands and sheared context from surge 10 samples.

The average *D* of smooth spherical vesicles is 0.023 (σ = 0.035), and the average *D* of rough spherical vesicles is slightly higher than their smooth surfaced counterparts, at 0.038 (σ = 0.038). Ellipzoidal vesicles all have $D > 0.1$ by definition, and the average *D*'s of smooth ellipzoidal and rough ellipzoidal vesicles are both slightly above 0.2, but range up to 0.73 and 0.51, respectively. The average *D* of sharp-tipped ellipzoidal vesicles is 0.50 (σ = 0.14) and range from 0.2 to 0.81. Both their average *D* and their minimum *D* value are the highest of the vesicle classes. The second highest average *D* is 0.42 (σ = 0.21) for stretched distorted vesicles. The average *D* of distorted vesicles is slightly below 0.2 (σ = 0.14). The maximum *D* values of all vesicle types (marked by the upper whiskers in Figure 3) is as high as ~0.8 (from sharp-tipped ellipzoidal and stretched distorted vesicles). Although with sharp-tip(s) absent, some smooth ellipzoidal vesicles are highly elongated, with a maximum *D* of 0.75, the third highest maximum values among all vesicle shapes.

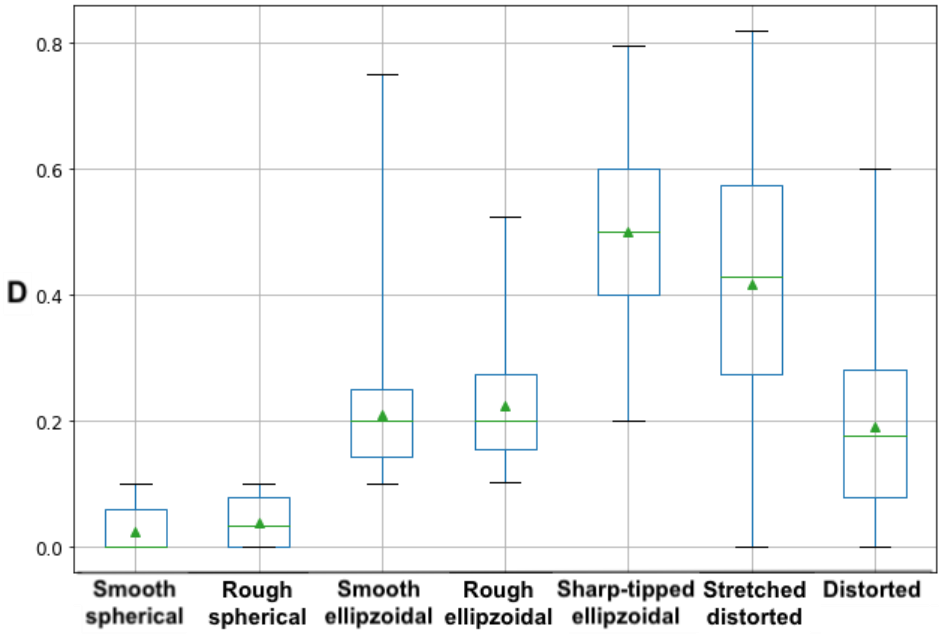

Figure 3: Box plot of deformation index (*D*) shown by vesicle types. Green triangles represent average *D* values for each vesicle type. The extents of upper and lower whiskers are maximum and minimum *D* values for each vesicle type, and green line is the median. Total number of vesicles measured and classified as smooth spherical, rough spherical, smooth ellipzoidal, rough ellipzoidal, sharp-tipped ellipzoidal, stretched distorted and distorted are 1030, 243, 1257, 348, 140, 24, and 205, respectively. The standard deviation of smooth spherical, rough spherical, smooth ellipsoidal, rough ellipsoidal, sharp-tipped ellipsoidal, stretched distorted, and distorted vesicles are 0.035, 0.038, 0.090, 0.092, 0.14, 0.21, and 0.14, respectively.

Clasts from 1991 Mt. Pinatubo pre-climactic surge deposits are typically dominated by two to three vesicle shapes, and in general the most common vesicle types are smooth spherical and smooth ellipzoidal (Figure 4; Table 6 & 7, appendix). Within individual clasts, the proportion of smooth spherical vesicles ranges from 10 % to ~80 % (average proportion of smooth spherical vesicles on clast basis ~30 %, $\sigma = \pm 14$ %), whereas smooth

ellipzoidal vesicles account for 20 – 65 % (average at 40%, σ = ±13 %) of vesicles (Figure 4; Table 6, appendix). Micron-scale heterogeneity is observed in most clasts. For example, in surge 10, some stretched and sharp-tipped vesicles are found next to smooth spherical and smooth ellipzoidal vesicles (Figure 2F).

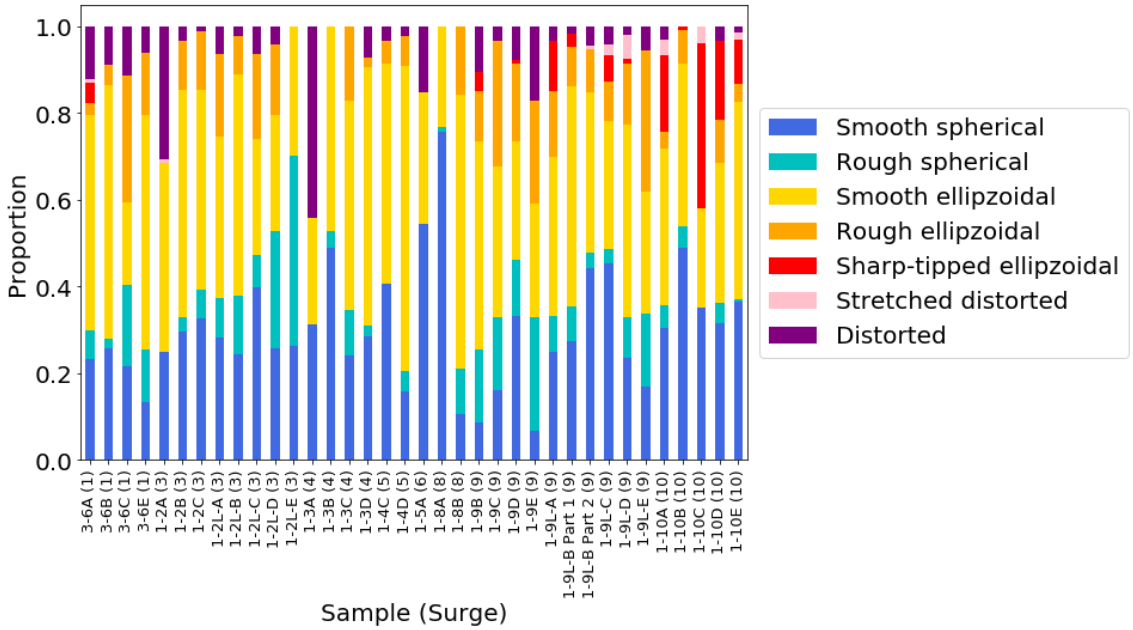

Figure 4: Proportions of vesicle types among measured vesicles in clasts from Mt. Pinatubo pre-climactic surges. Each bar represents a clast analyzed in terms of vesicle texture.

The dominant vesicle shapes vary from clast to clast within single surge events. In surge 4, for instance, sample 1-3A contains 44 % distorted vesicles, 31 % smooth spherical, and 25 % smooth ellipzoidal vesicles. In contrast, another sample from surge 4 (1-3B), has no distorted vesicles, but a few % of rough spherical and nearly 50 % and 50 % of smooth spherical and smooth ellipzoidal vesicles (Figure 4; Table 6, appendix).

The most striking difference we observed occurs between surge events. There is a progressive change in proportions of vesicle shapes from a near absence of sharp-tipped ellipzoidal vesicles and very few stretched distorted vesicles in earlier surges to a significant population of sharp-tipped ellipzoidal and stretched distorted vesicles in surge 10 (Figure 2F-H; Figure 4). Sharp-tipped ellipzoidal vesicles are nearly absent in clasts from the earlier surges, but make up as much as 12 % of vesicles in clasts from surge 9 and up to 38 % in clasts from surge 10 (Table 6 & 7, appendix). Stretched distorted vesicles also increase in abundance from ~0.1-0.3 % in early surges to up to 6 % in clasts from surges 9 and 10. There is also an increased stretching of vesicles represented by change in clast average D values (Table 4; Figure 5). Eighteen out of nineteen clasts from surge events before surge 8 all have an average $D < 0.16$, whereas seven out of seventeen clasts deposited in surges 8, 9, and 10 have average $D > 0.16$. Three clasts from surge 10 have clast average D close to or greater than 0.2. In most cases larger vesicles tend to be more deformed and smaller vesicles tend to be more rounded. In surge 10, we observed numerous small vesicles that are stretched and distorted.

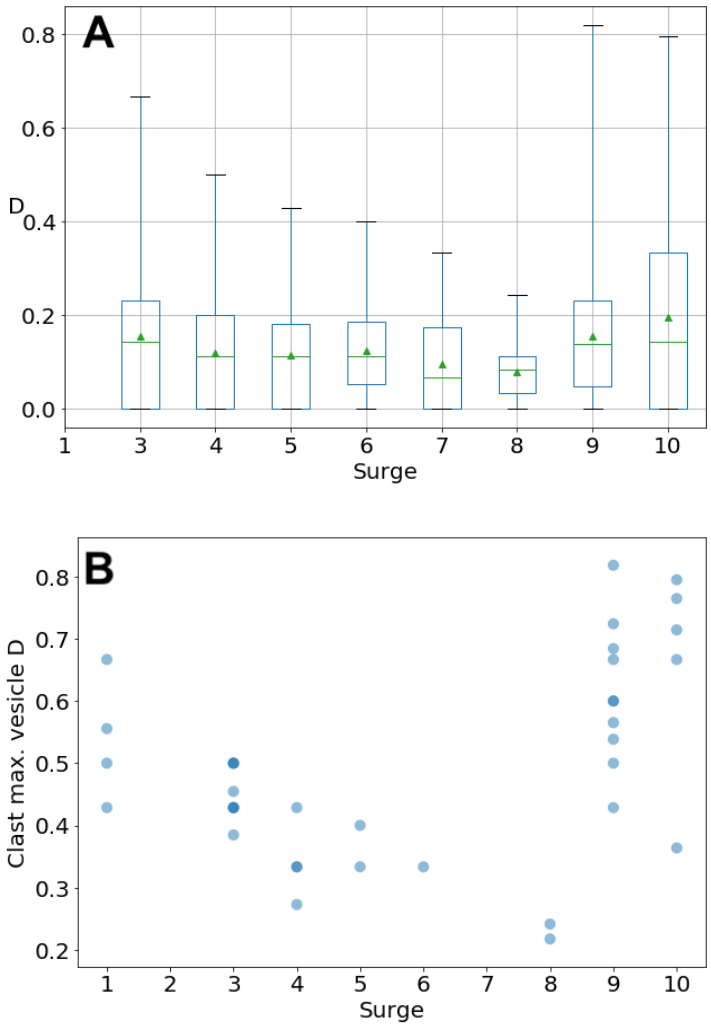

Figure 5: **A** Deformation index (*D*) of vesicles measured in the 1991 Mt. Pinatubo pre-climactic dense cognate lithics. Total number of vesicles measured in surges 1, 3, 4, 5, 6, 8, 9, and 10 are 373, 773, 226, 103, 46, 118, 919, and 689, respectively. Whiskers cover full range of *D*'s. Green line and green triangle represent median and mean values, respectively. **B** Maximum deformation indices (*D*'s) measured in clasts from the 1991 Mt. Pinatubo pre-climactic dense cognate lithics. Each circle represents a single clast. Numbers of clasts from surges 1, 3, 4, 5, 6, 8, 9, and 10 are 4, 8, 4, 2, 1, 2, 10, and 5, respectively. The darker color represents circles overlapping.

Another distinguishing feature of vesicle shapes through surges is an increased proportion of rough spherical and rough ellipzoidal vesicles in surge 9 (Figure 4; Table 6

& 7, appendix). Rough spherical and rough ellipzoidal vesicles are not common in most surges. Together, the two rough surfaced vesicle types make up 21 % of vesicles in surge 1, and 24 % in surge 3 (Table 7, appendix). All other surges contain less than 10 % of these two vesicle types combined. In surge 9, however, over 28 % of vesicles have rough surfaces.

VESICULARITY

Vesicles usually show heterogeneity in spatial distribution and occur in clusters in clasts with vesicularity up to 45 vol.%. Although more vesicular clasts have more uniform vesicle distribution (Figure 2A), most clasts contain sub-domains with no vesicles and other sub-domains with vesicularity up to ~65 vol.%. Higher vesicularity is usually observed in vicinity of large phenocrysts or in matrix glass bounded by phenocrysts (Figure 6), compared with matrix glass farther from large phenocrysts. The higher vesicularity results from a combination of higher vesicle number densities and larger vesicle sizes. As an example, pockets of vesicles around phenocrysts can reach up to 65 vol.% in sample 1-2A from surge 3, whereas the clast bulk vesicularity is 28 %. Similar textures are found around fractured hornblende phenocrysts, where rounded vesicles are found in hornblende cracks and sometimes along cleavage planes, whereas matrix glass surrounding the hornblende phenocrysts is much less vesicular or in some cases free of vesicles.

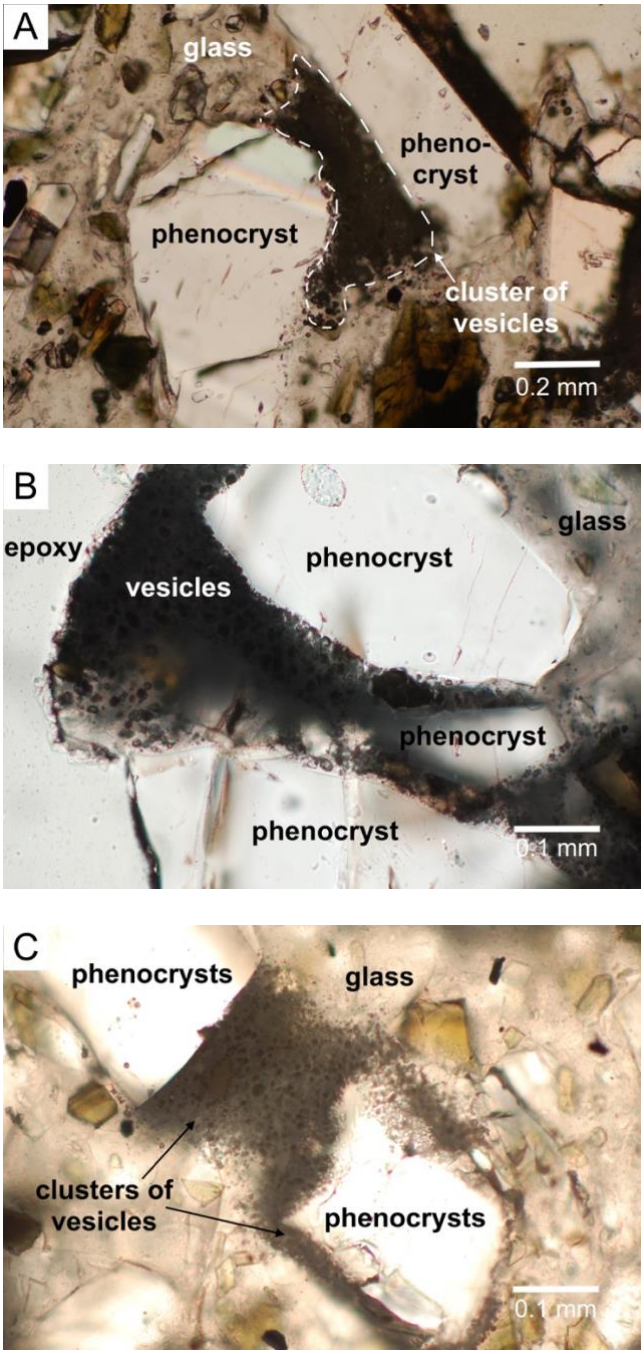

Figure 6: Optical microscope images showing clusters of vesicles around large phenocrysts in Mt. Pinatubo dacite lithic samples.

Bulk vesicularity varies within individual surge deposits but are mostly within a range of 30 vol.% (Figure 7). Clasts from all surges have vesicularities less than 50 vol.%, with minimum measured ~0 vol.%, except for one clast from surge 9 (sample 1-9L-E), which has bulk vesicularity of ~80 vol.%. There is no trend in variation of bulk vesicularity through the surge events.

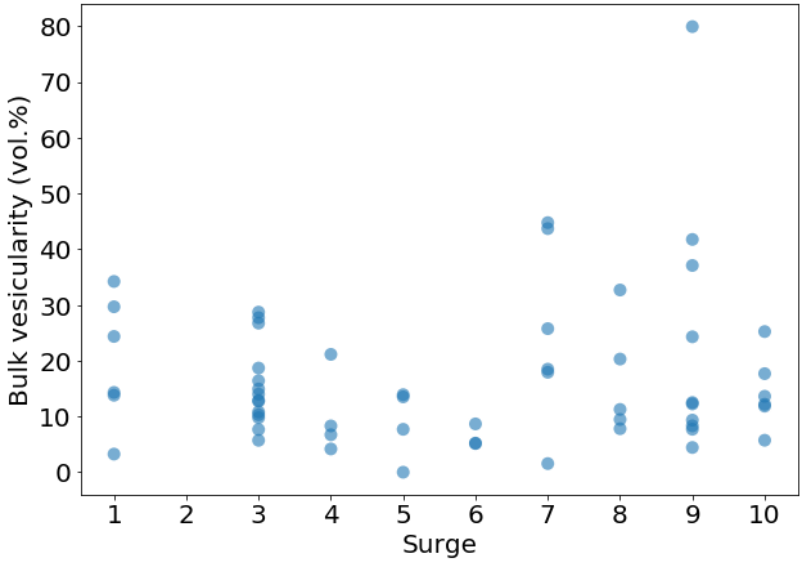

Figure 7: Bulk clast vesicularity of the 1991 Mt. Pinatubo pre-climactic dense cognate lithics measured from BSE images. Number of clasts measured from surges 1, 3, 4, 5, 6, 7, 8, 9, and 10 are 7, 13, 4, 4, 3, 6, 5, 12, and 5, respectively.

VESICLE SIZE AND *D*

Vesicle sizes vary widely within the 1991 Mt. Pinatubo pre-climactic dense cognate lithics. Vesicle widths instead of lengths are used to characterize vesicle size in general, because it is less affected by stretching and elongation of vesicles. It is common to find 1-2 μm sized, smooth-spherical vesicles in dense glass in almost all samples, whereas

vesicles tens of microns in width also occur in most clasts. Average vesicle width within individual clasts range from ~3 μm (surge 10; Table 4) up to ~17 μm (surge 9). The large variation is represented by the high standard deviations of vesicle widths (Table 4). As an example, clast average vesicle widths from surge 9 have standard deviation as high as 8.2 μm, whereas the average is 16.9 μm. The largest vesicles found in surge 1 to surge 6 show a decreasing trend in size, from 33 μm in surge 1 to 7.5 μm in surge 6 (Figure 8). The averages of vesicle widths from surge 1 to surge 6, on the other hand, do not show a distinguishing trend and are all below 8 μm. Surge 8 contains clasts with the largest vesicles in general compared with other surges, with the average vesicle width close to 15 μm (σ = 2.92). The magnitude of ranges of vesicle widths observed in individual surge events are somewhat associated with total number of observations, i.e., total number of vesicles measured. For example, vesicles from surge 6 (with only 46 vesicles measured) show a cluster in width and span only a few microns from maximum to minimum widths. Surge 9, on the contrary, has 919 width measurements that span from 1 μm to 40 μm. Given that measured vesicle width ranges are partly dependent on sample size, surge 3 and surge 10 have a relatively uniform distribution in vesicle widths, with the significantly large sample sizes (773 and 689 total vesicles measured, respectively) and relatively small span of vesicle widths (~20 μm for both surges). Surge 3 is characterized by an average vesicle width of ~7 μm, and maximum vesicle width ~22 μm. Surge 10 produced relatively small vesicles compared to most of other surges, with an average vesicle width ~4 μm and the largest observed vesicle ~20 μm in width.

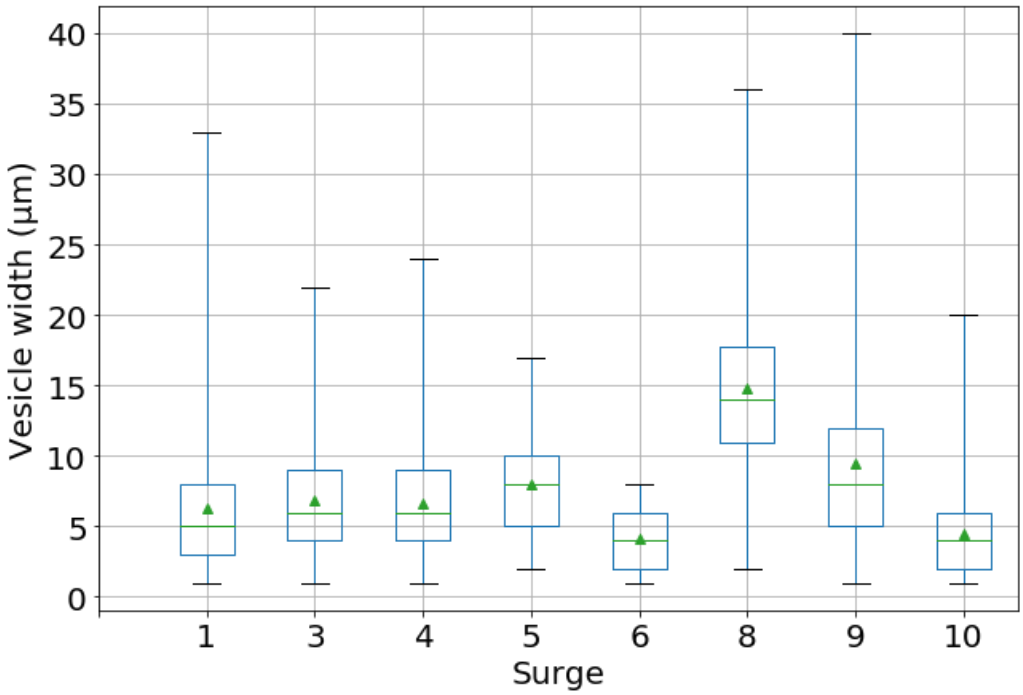

Figure 8: Vesicle widths from the 1991 Mt. Pinatubo pre-climactic dense cognate lithics. Total number of vesicles measured in surges 1, 3, 4, 5, 6, 8, 9, and 10 are 373, 773, 226, 103, 46, 118, 919, and 689, respectively. The associated standard deviations for each surge are 2.59, 1.98, 1.93, 1.91, 1.07, 2.92, 2.90, and 1.54, respectively.

H_2O AND CO_2

Dissolved H_2O and CO_2 concentrations from the eight studied surges range from 0.56 to 2.58 wt.%, and from 4 to 35 ppm, respectively (Figure 10; Table 5). The data overlap those reported by Hammer et al. (1999). Dissolved volatile concentrations in matrix glass of the 1991 Mt. Pinatubo pre-climactic dense cognate lithics are extremely variable. Measured concentrations of H_2O and CO_2 within single clasts span can range up to 1.26 wt.% and 18 ppm, respectively (Table 10, appendix). Volatile heterogeneity within clasts is highlighted by a clast (1-2L-B) from surge 3, where clast average H_2O and CO_2

are 1.3 wt.% and 19 ppm, respectively. Within the clast, on one side of a hornblende phenocryst, H_2O and CO_2 are measured to be 0.59 wt.% and 12 ppm, respectively, whereas matrix glass 500 μm away, on the other side of the same hornblende phenocryst, contains 1.49 wt.% H_2O and 22 ppm of CO_2.

surge event	n. analyses (H_2O)	min. H_2O (wt.%)	max. H_2O (wt.%)	avg. H_2O (wt.%)	n. analyses (CO_2)	min. CO_2 (ppm)	max. CO_2 (ppm)	avg. CO_2 (ppm)
1	9	1.01	1.44	1.30 (0.15)	3	7.26	10.29	8.68 (1.52)
3	73	0.59	2.13	1.60 (0.30)	73	9.26	35.36	22.17 (5.37)
4	36	1.41	2.46	1.81 (0.23)	36	10.02	27.00	17.82 (4.49)
5	30	1.22	2.15	1.82 (0.20)	30	10.55	29.00	16.91 (4.40)
6	10	1.32	2.00	1.55 (0.26)	10	13.08	27.07	20.39 (4.24)
8	32	1.21	2.58	1.61 (0.27)	31	4.63	30.35	15.12 (7.25)
9	82	0.56	2.35	1.48 (0.31)	59	4.00	22.20	10.08 (3.72)
10	54	0.62	2.18	1.40 (0.28)	34	4.20	10.45	6.72 (1.40)

Table 5: Dissolved H_2O and CO_2 concentrations in matrix glass of 1991 Mt. Pinatubo pre-climactic dense cognate lithics.

The average H_2O and CO_2 contents in the 34 cognate lithics are 1.56 ± 0.21 wt.% and 14.2 ± 2.9 ppm, respectively, based on average concentrations from 34 clasts (Table 4). Average H_2O concentrations from all clasts fall within 1-2 wt.%. Within individual surge events, average H_2O concentrations vary slightly, but never exceed 0.7 wt.% (largest variation observed in surge 9; Table 4). Variations in clast average CO_2 concentrations within single surge events are all below 10 ppm, except for surge 8 (Table 4).

Across surge events, we see no significant change in H_2O concentrations, but a significant decrease in CO_2 in the later surges (Figure 9; Figure 10). Average dissolved CO_2 concentrations decrease from ~22 ppm in surge 3 to < 7 ppm in surge 10. The trend is significant because of the number of spot analyses, especially on surges 9 and 10. Although a significantly number of measurements (59) were made on surge 9 samples, the maximum still lies below 22. Clasts from surge 10, yields highly clustered dissolved CO_2

concentrations that are all between ~5 and ~10 ppm. Clasts from surge 1 are also poor in dissolved CO_2 concentration (~8 ppm), but the limited number (3) of analyses makes the average value suspect.

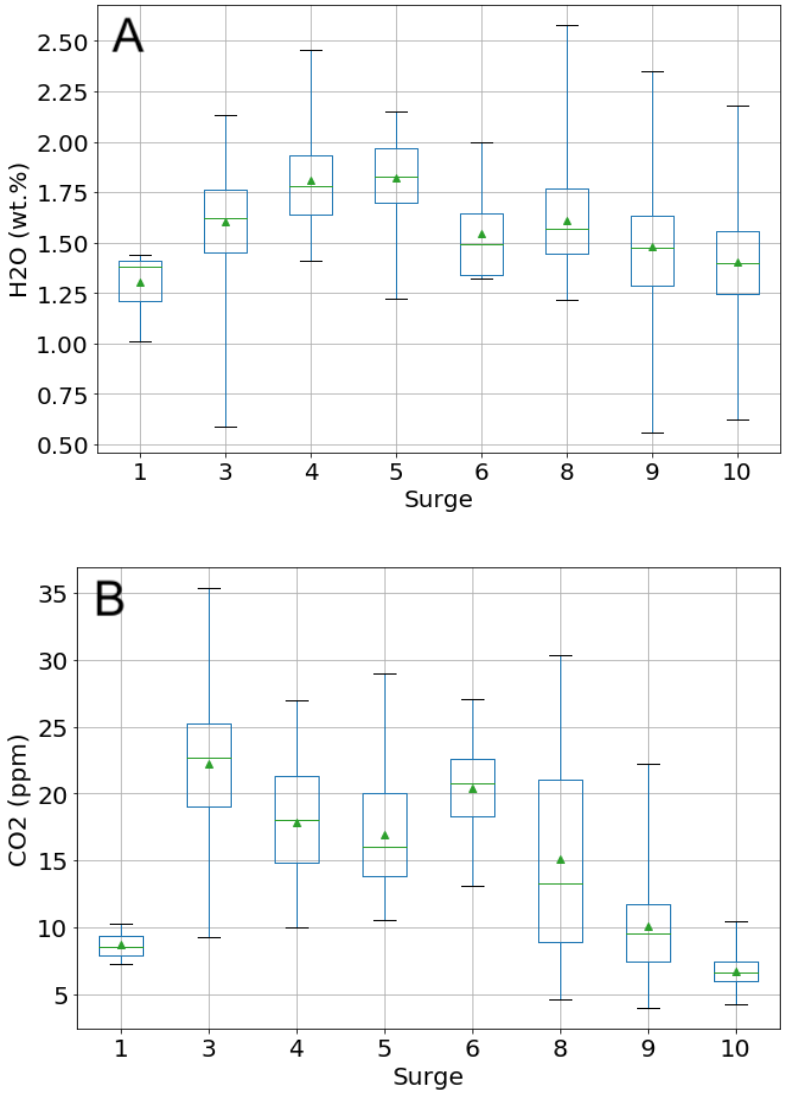

Figure 9: H_2O (**A**) and CO_2 (**B**) concentrations from all measurements on 1991 Mt. Pinatubo pre-climactic dense cognate lithic clasts. Green triangles represent average values of all measurements within a single surge event. Number of measurements and standard deviations are reported in Table 4.

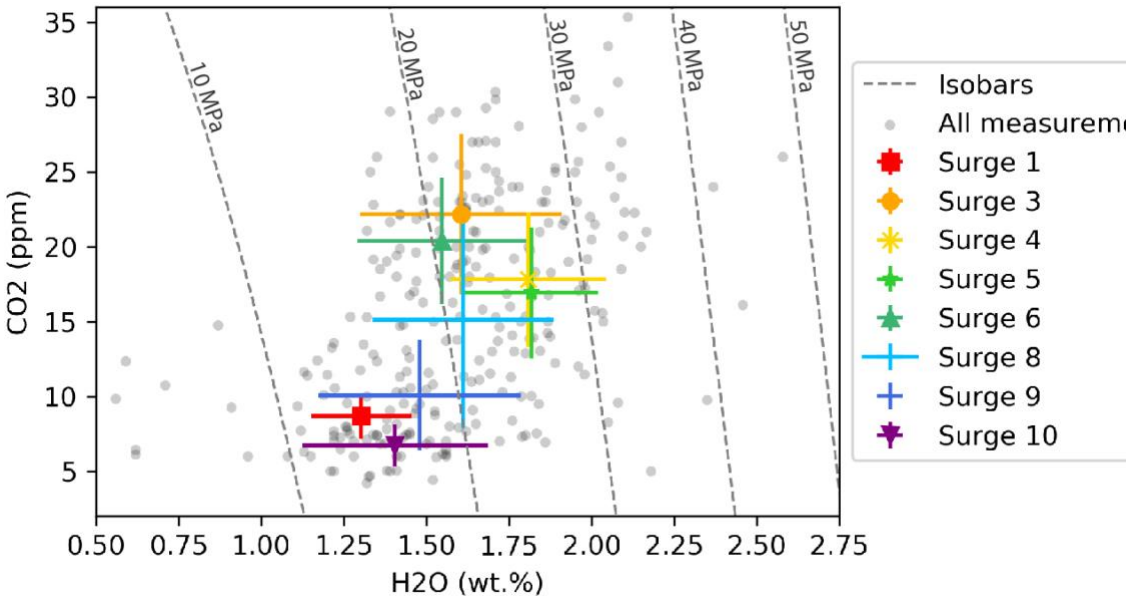

Figure 10: Measured concentrations of dissolved volatiles in dacite lithic clasts from 1991 Mt. Pinatubo pre-climactic surge deposits. Grey circles are all the spot analyses from original FTIR measurements. Colored markers with error bars represent surge average CO_2 and H_2O. Error bars in both directions represent 1 σ of average for all analyses in that surge. Dashed curves are isobars and isopleths (curves of constant equilibrium vapor composition) assuming a magmatic temperature of 780 ^oC (Liu et al., 2005).

CRYSTALS AND CRYSTAL FRAGMENTS

Bulk crystallinity of the dense cognate lithics falls in a range between 40 % and 60 % (Table 4). The majority of the crystallinity is accounted by phenocrysts, which are composed of feldspars (15 – 20 modal %), hornblende and cummingtonite (15 - 20 modal % combined), quartz (up to 10 modal % in some clast and absent in others) and minor proportions of biotite (up to 5 modal % in some clasts and absent in most clasts), apatite (<5 modal %) and oxides (~5 modal %). Larger phenocrysts are up to ~2 mm in size, with

some fractured. Many intact or broken pieces of plagioclase feldspar phenocrysts show zoning.

In addition, tiny pieces of crystal fragments are numerous and ubiquitous in dacite lithic samples (Figure 11A-C, E), showing random distribution and large variation in size throughout matrix glass. Crystal fragments typically bear no crystal habit and show sharp edges regardless of size. Pale-green shards of hornblende fragments are common (Figure 11B) in addition to low-relieved colorless feldspar counterparts. The crystal assemblage of these crystal fragments thus resembles that of phenocrysts.

Microlites are observed using optical microscope and using scanning electron microscopy. Larger microlites with area > 150 μm are identified in clasts from surge 1 deposit using optical microscopes. They are typically rectangular in shape with slightly curved edges on two ends (Figure 11C). Feldspar microlites with long axis less than 5 μm are observed in clasts from surge 4 and 5, using SEM (Figure 11E, F), with some occurring in swallow-tailed elongated form and show no preferred orientation in matrix glass.

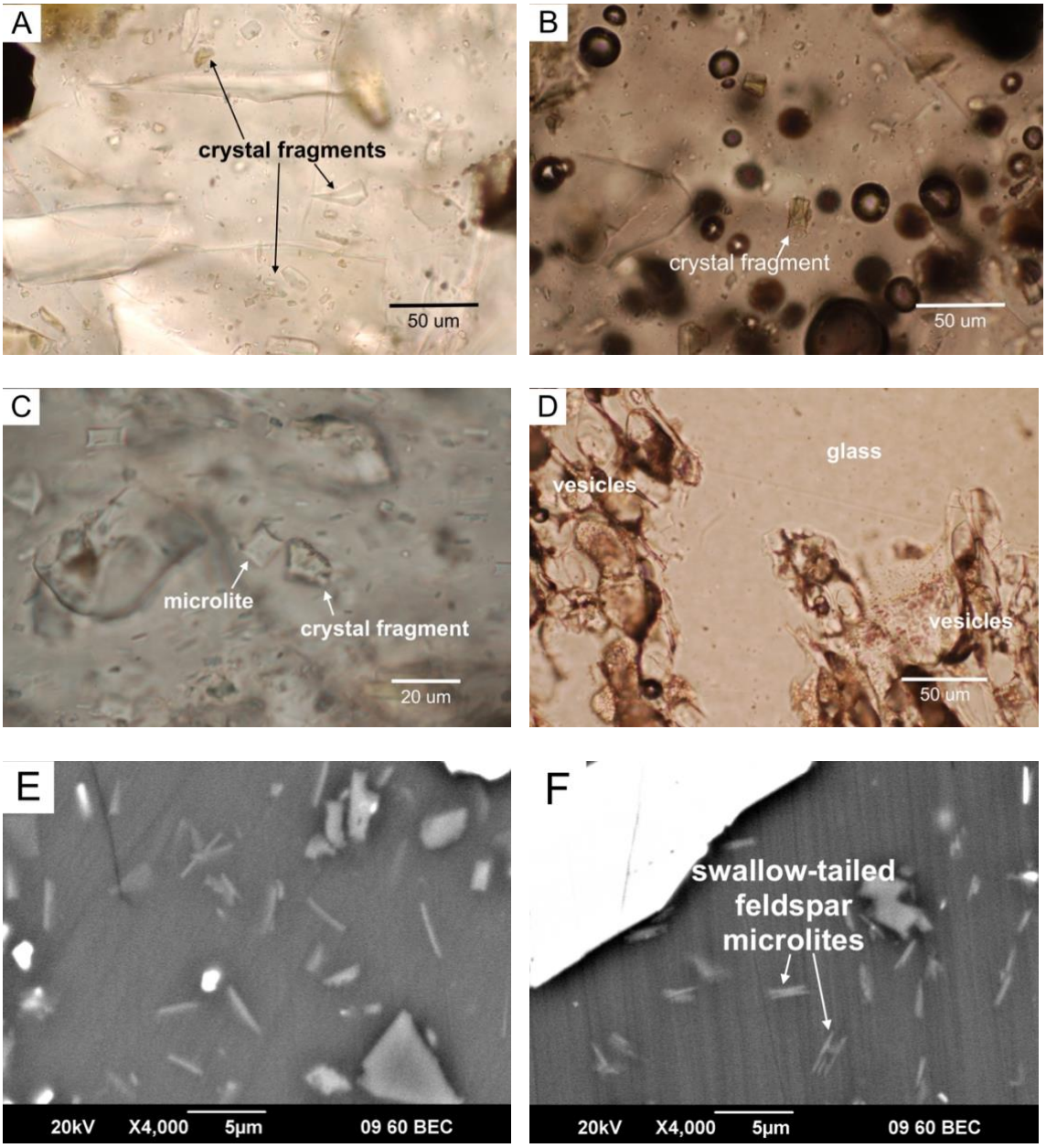

Figure 11: Optical microscope (**A-D**) and SEM images (**E & F**) of crystal fragments (**A-C, E**) and microlites (**C, E, & F**) in 1991 Mt. Pinatubo dacite lithics deposits, and microlite and crystal fragment free glass in dacite pumice deposit (**D**, sample P351 from Hammer, 1999). Clasts from A-F are from surge events 10, 8, 1, 3, 4, and 5.

DACITE PUMICE

The pumice sample (P351) from surge 3 is highly vesicular, with clear matrix glass free of crystal fragments (Figure 11D). Vesicles and phenocrysts make up ~40 and ~20 % of whole clast, and crystallinity is ~50 %. CT data on the pumice sample from surge 3 (P1-2A) yields a bulk crystallinity of 48 %, and the one from surge 9 (P1-9A) yields 24 %. Phenocryst phases observed include plagioclase feldspar, quartz, and hornblende.

Discussion

Textural observations on the 1991 Mt. Pinatubo surge-producing eruptions serve as an extraordinary window for the investigation of pre- and syn-explosive conduit dynamics, thanks to well logged eruption time scale, which is a significant factor in the investigation of how the observed texture come into existence. The thirteen 1991 Mt. Pinatubo pre-climactic surge events were observed to have occurred more frequently (Table 2), so that repose intervals between events decreased from the initial 2-3 hrs at the beginning of the series to around 20 mins just before the climactic eruption (Hoblitt et al., 1996).

Petrographic study on microlite size and population are observed to correlate with repose durations in the 1991 Mt. Pinatubo pre-climactic eruptions (Hammer et al., 1999). Such correlation results from observations that devolatilization of a rhyolitic melt from ~6.5 wt.% to 0.1-1 wt.% H_2O can result in significant undercooling of up to 200^oC (Swanson, 1977), triggering crystallization (Eichelberger et al. 1986). A correlation of maximum microlite abundance with repose interval is observed by Hammer et al. (1999) in 1991 Mt. Pinatubo pre-climactic dense dacite clasts, where clasts produced by surges preceded by short repose intervals (< 40 mins) are microlite free. Nucleation and growth of microlites and by inference the formation of pre-climactic lithic materials, must have occurred within the timeframe restrained by the pre-climactic eruption series and the hiatus intervals, which would be minutes to hours (Table 2).

Hoblitt et al. (1996) observed that the dominant petrology of the 1991 eruption deposits display a chronological trend from mostly andesite in earlier deposits to mostly dacite in later deposits, to pure dacite in the climactic eruption on June 15, 1991, and suggested a magma mixing model in response to the petrological evolution. The possibility that the observed textures in the surge-deposited dense cognate dacite are from magma

mixing between the basaltic and dacitic end members of magmas is eliminated, because of the dacitic mineralogy of phenocrysts and crystal fragments, and the consistently rhyolitic composition of matrix glass.

Any model that describes the formation of the dacite lithics must operate over a time frame of minutes to hours. Most importantly, any model must explain the following observations within that time frame. First, the ubiquitous occurrence of crystal fragments observed in all dacite lithic samples requires fragmentation before formation of the dense lithics. Second, sub-millimeter scale heterogeneity in H_2O may reflect 1) highly variable conditions sub-domains of clasts originated and/or partially degassed at, thus various depths or duration of stalling 2) insufficient time for intra-clast volatile diffusion and equilibration. Third, the highly variable vesicularity and shifts in dominating vesicle shapes also point to various extents of degassing or formation processes that allow for coalescence of distinct texture before eruptive processes.

Previous models argue that non-explosive silicic eruptive products form as magma vesiculation creates a permeable foam, followed by degassing and foam collapse (Eichelberger et al., 1986). Such a model cannot explain many textures we observed in the 1991 Mt. Pinatubo pre-climactic surge deposits. First, foam collapse model does not involve fragmentation processes within volcanic conduits, and thus cannot account for the ubiquitous occurrence of crystal fragments. Second, permeable foams are spatially continuous and thus would not be expected to have volatile contents that are spatially variable at a scale of tens of microns. Lastly, we used the viscosity model of Hess and Dingwell (1996) to calculate melt viscosity:

$$\log \eta = [-3.545 + 0.833\, In(w)] + [9601 - 2368\, ln(w)]/(T - [195.7 + 32.23\, ln(w)]) \quad (2)$$

where η is viscosity in Pa s; w is dissolved water concentration in wt.%, and the clast average of 1.56 wt.% is used to represent Mt. Pinatubo melt; T is temperature in kelvins, which is 1053.15 K (780 °C; Scaillet and Evans, 1999) for pre-eruptive Mt. Pinatubo magma. Melt viscosity is thus $10^{6.96}$ Pa s (range between $10^{6.14}$ Pa s and $10^{8.50}$ Pa s if using minimum and maximum values from individual spot analyses for dissolved water concentrations) for Mt. Pinatubo dacite lithics. If crystal content is included, the bulk viscosity is expected to be much higher. At such viscosities, rhyolitic foam is expected to take $>10^4$ hours to collapse, based on the experimental results of Martel and Iacono-Marziano (2015; Figure 12), inconsistent with observations of these eruptions.

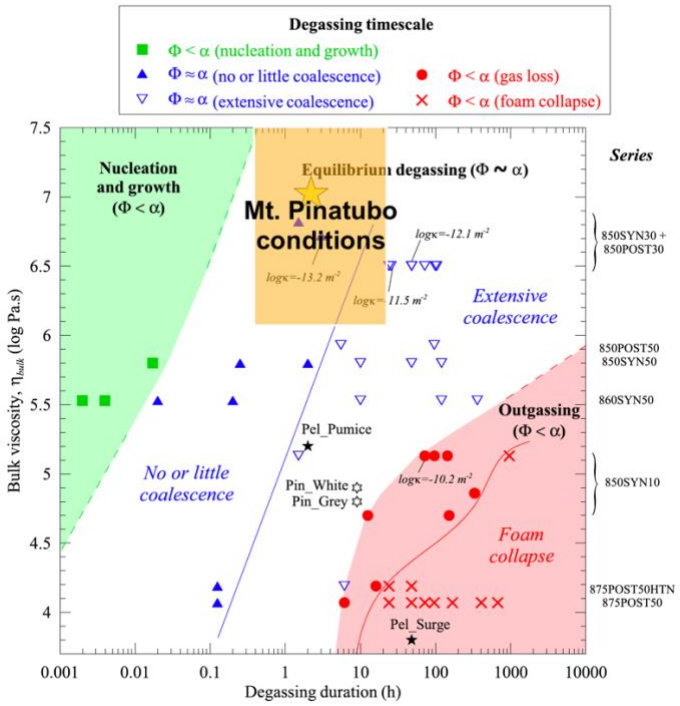

Figure 12: Effect of the viscosity of the bubbly melt on the degassing timescale. Viscosities are calculated using eq. (2). Yellow star represents average melt conditions forming Mt. Pinatubo dense cognate lithics. Orange box covers the whole timescale of Mt. Pinatubo surge events and range in H_2O. Figure after Martel and Iacono-Marziano (2015).

Here we propose an ash particle sintering model to explain the formation of dense dacite in short periods of time. After magma fragments into ash, the ash particles collide and sinter onto the conduit walls in a repetitive manner. Pieces of the wall material can be reincorporated into the eruption to collide and resinter again, before finally erupting. Sintering being the main mechanism forming dense pyroclasts is supported by the following 3 lines of evidences. First, the ubiquitous occurrence of crystal fragments in dense dacite lithics requires fragmentation of pre-existing crystals and suturing and annealing to reincorporate them into the final melt. Second, the heterogeneity of H_2O and CO_2 contents in matrix glass within 500 μm indicates that sub-domains within each clast equilibrated at significantly different depths. Similar ranges of H_2O from clasts from different surges could represent the repeated process of ascending ash particles from various depths stalling on conduit wall, sintering, shattered and re-incorporated in ascending ash that eventually stalls again at different depths before ejection. Third, the significant variations in vesicle textures within clasts are expected if various sub-domains sinter together, based on experimental evidences (Gardner et al., 2019).

The dacitic mineral assemblage of observed crystal fragments and their absence in dacite pumice indicate that they are broken pieces of phenocrysts from the juvenile magma that are later reincorporated into the erupting melt. This is different from the origin of the "xenolith" and "xenolith powder" observed by Rust and Cashman (2007) in pyroclastic deposits of the 1300 B.P. eruption of Newberry Volcano. The xenoliths are inferred to be incorporated wall rock materials that give rise to higher dissolved CO_2 in the interstitial melt, whereas we observe no association between abundance of crystal fragments and dissolved CO_2 contents in the Mt. Pinatubo dense dacite lithics.

The abundance of stretched and sharp-tipped types of vesicles indicates shearing before cooling and potentially represents textures preserved from the interaction between

ash particles and the conduit walls during the sintering process. The elevated proportions of sharp-tipped ellipzoidal vesicles and stretched distorted vesicles in surge 9 and particularly surge 10 (Figure 2F-H; Figure 4) parallel their short hiatus times (~40 mins and ~30 mins respectively), as opposed to hiatus times of earlier surges that are >100 mins and up to 262 mins (Table 2). This further supports the sintering model and indicates that formation of observed textures and dense dacite lithics happened at the scale of eruption timeframe.

The micron-scale heterogeneity in vesicle types resembles that in volatile concentrations. With the increased abundance of the more sheared types of vesicles in surge 10 deposit, smooth spherical (35.9 %) and smooth ellipzoidal (36.4 %) vesicles, although smaller in size compared with their counterparts in earlier surges, are still the dominating vesicle types and can occur microns away from sharp-tipped ellipzoidal vesicles. The heterogeneity in vesicle types reflects: 1) sintering of ash particles sourced from various depths or have stalled for different durations that allowed different degrees of relaxation, or 2) dynamics in particle welding processes where vesicles on the interiors of hot ash particles experience less inter-particle collision and shearing whereas vesicles at particle fringes are more sheared with lower temperature thus higher viscosity hindering relaxation.

The heterogeneity in vesicle distribution is produced by sintering experiments by Gardner et al. (2019). Rhyolitic obsidian was sintered using bimodal mixture of "finer" and "coarser" ash particles, with the coarse particles having principle axes of 696 ± 244, 429 ± 73, and 212 ± 81 μm, and fine particles having principle axes of ≤ 2 to 45 μm in size. A mixture of 50 wt.% and 50 wt.% of coarse and fine ashes produced clasts showing clusters of vesicles in the vicinity of relict large particles after 45 mins of sintering at 22 MPa and 750 ^{o}C (Gardner et al., 2019). Furthermore, closer spacing of coarse particles results in

larger vesicles (up to 600 μm) and higher porosity (26 vol.%), whereas with coarse particles farther apart, matrix that used to contain fine ash is only about 4 vol.% porous (Gardner et al., 2019). The course particles resemble many phenocrysts observed in the dense dacite lithics in terms of size, and vesicle pockets clustering around coarse particles are analogous to vesicles clustering around phenocrysts in natural dense dacite samples.

Experimental studies on sintering processes conducted by Gardner et al. (2018) can be used to constrain the timeframe on formation of the dense cognate lithics under the sintering model. The experimental conditions used by Gardner et al. (2018; 700 – 800 ^{o}C, isobaric H_2O pressure at 20 and 40 MPa) resemble shallow conduit conditions where obsidian powders with two different size distributions sinter and evolve in texture within a timeframe of minutes to hours. Four phases are identified from sintering products (Gardner et al., 2018): 1) particles loose and lack cohesion; 2) particles are sintered at their contacts but are interpenetrated by continuous tortuous pore space; 3) porosity is no longer fully connected, with isolated spherical vesicles and networks or larger vesicles that remain multicuspate in shape and 4) dense glass with fully isolated spherical vesicles and maybe a few larger complex-shaped ones. Figure 13 shows evolution of textures from sintered products with sintering time and variation in melt viscosity. Given that the average Mt. Pinatubo pre-climactic dacite lithics has a viscosity of ~$10^{6.96}$ Pa s, textures from sintering between ~40 to >200 mins (Mt. Pinatubo eruption timeframe) can produce vesicular products in the domains of phase 3 and phase 4, which mimic what we observed in the dense dacite lithics.

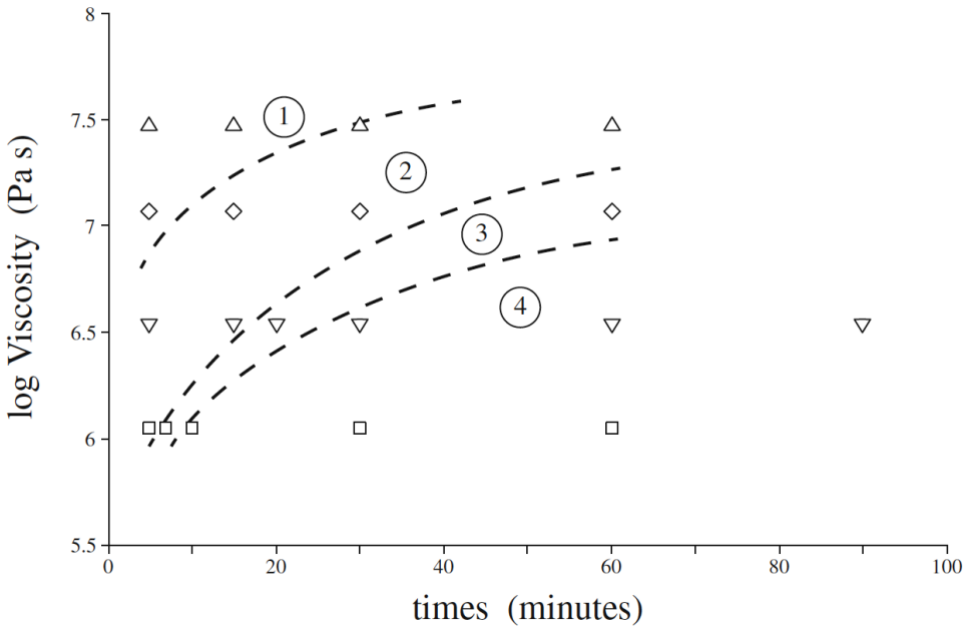

Figure 13: Variations in sintering texture of un-sieved samples as a function of equilibrium melt viscosity. Numbers in circles represent phases sintered products belong to. Dashed lines separate approximate fields of constant texture. Figure after Gardner et al. (2018).

The clast average CO_2 concentrations progressively decrease from ~22 ppm in early Mt. Pinatubo surge events to ~7 ppm in surge 10. Similar variations have been seen in other magmatic systems, such as the Newberry Volcano (Rust and Cashman, 2007) and Mono Craters (Rust et al., 2004; Gardner et al., 2017). Various models have been proposed, including gas fluxing (Rust et al., 2004) and non-equilibrium vesiculation (Gonnermann and Manga, 2005). The observed decreasing trend in CO_2 gives rise to a decrease in CO_2/H_2O ratio in the later more frequent surge events, given the relatively constant H_2O concentrations. This contradicts the slower diffusion of CO_2 relative to H_2O (Gonnermann and Manga, 2005) because a higher CO_2/H_2O ratio is expected instead in response to the

shorter degassing time. The observed decreasing trend of CO_2 concentrations is not correlated with vesicularity (degrees of volatile exsolution) or intensity of surge eruptions. It thus cannot be explained by closed system degassing. Furthermore, the trend does not correlate with abundance of crystal fragment like is observed in Newberry Volcano deposits (Rust and Cashman, 2007). We thus suggest that the trend represents various amounts of CO_2 in a fluid phase released from the intruding basalt that is later mixed into the dacitic magma. As the amount of mafic magma decreased chronologically during the eruption series, until its complete absence in the climactic eruption (Hoblitt et al., 1996), the associated amount of CO_2 released decreases correspondingly. The decreasing trend has to come from change in amount of a separate fluid phase, instead of an inter-surge shift in melt composition because the composition of interstitial glass is consistently rhyolitic (SiO_2 between 77 and 79 wt.%) throughout surge events.

Conclusions

Dense dacite lithics from the 1991 Mt. Pinatubo pre-climactic eruptions provide a window into pre- and syn-eruptive conduit dynamics. Sub-millimeter scale crystal fragments with sharp edges and irregular form are scattered in the 1991 Mt. Pinatubo pre-climactic surge deposits, reflecting a re-incorporation mechanism after fragmentation in shallow conduit. We found the mineralogy of crystal fragments to resemble phenocryst materials and infer that the source of these pieces of shards not to be wall-rock material, but sutured pieces of pre-existing phenocrysts from the ascending magma.

Vesicle shapes are classified and are used to represent domains with various degrees of sheering and relaxation. While the most dominant vesicle shapes are spherical and rounded ellipsoid, there is a significant increase in the population of sharp-tipped ellipsoid vesicles and stretched-distorted vesicles from the earlier surge producing events to surge 9 and 10. The preserved sheered texture is due to an in general shorter stalling time on conduit walls for the sintered ash products to fully relax before eruption during the more frequent surge events of the 1991. Mt. Pinatubo eruptions.

Vesicularity and vesicle size are heterogeneous in the 1991 Mt. Pinatubo pre-climactic dacite lithics, which reflects a variation in the origination and degassing history of sub-domains of erupted products. Vesicles tend to cluster around large phenocrysts which give rise to higher zonal vesicularity, representing a feature caused by heterogeneous particle sizes between phenocrysts and ascending ash particles that eventually sintered together.

Volatile data on H_2O and CO_2 provide insights on vesicle texture, evolution of degassing signature with eruption series, and help constrain pressure and depths of conduit processes. Although no distinguishing trend in H_2O is observed with the evolution of

eruption nor with vesicle texture, its greatly heterogeneous signature in sub-millimeter scale help eliminate the possibility that the eruption products formed by foam collapse. Average dissolved H_2O in Mt. Pinatubo melt is ~1.56 wt.% which give rise to a highly viscous melt with a viscosity of $10^{6.96}$ Pa s and extremely low possibility for the dense lithics to form within eruption timescale under the permeable foam hypothesis. Furthermore, with interstitial glass being consistently rhyolitic throughout the pre-climactic surges, CO_2 decreased to less than 10 ppm in the last few surges, indicating a waning input of a separated fluid phase enriched in CO_2 sourced from the basaltic counterpart of the two magma mixing end members.

With the observed textures, we eliminate the possibility that the permeable foam model is responsible for the formation of the dense cognate lithics produced from the 1991 Mt. Pinatubo pre-climactic surges. We conclude that these lithic materials are formed by sintering ash particles at various depths above the fragmentation level within the conduit in a repetitive manner. The occurrence of similar textures and crystal fragments observed in the 1300 B.P. eruption of Newberry Volcano (Rust and Cashman, 2007) and the ca. 1325-1350 C.E. North Mono eruptions (Gardner et al., 2017) expand the sintering model to a more general scheme which can potentially be applied to the formation of pyroclastic materials from other volcanic eruptions.

Appendix

sample	surge event	n. total	smooth spherical (%)	rough spherical (%)	smooth ellipzoidal (%)	rough ellipzoidal (%)	sharp-tipped ellipzoidal (%)	stretched distorted (%)	distorted (%)
3-6A	1	107	0.23	0.07	0.50	0.03	0.05	0.01	0.12
3-6B	1	89	0.26	0.02	0.58	0.04	0.00	0.00	0.09
3-6C	1	79	0.22	0.19	0.19	0.29	0.00	0.00	0.11
3-6E	1	98	0.13	0.12	0.54	0.14	0.00	0.00	0.06
1-2A	3	108	0.25	0.00	0.44	0.00	0.00	0.01	0.31
1-2B	3	88	0.30	0.03	0.52	0.11	0.00	0.00	0.03
1-2C	3	89	0.33	0.07	0.46	0.13	0.00	0.00	0.01
1-2L-A	3	110	0.28	0.09	0.37	0.19	0.00	0.00	0.06
1-2L-B	3	45	0.24	0.13	0.51	0.09	0.00	0.00	0.02
1-2L-C	3	108	0.40	0.07	0.27	0.19	0.00	0.00	0.06
1-2L-D	3	93	0.26	0.27	0.27	0.16	0.00	0.00	0.04
1-2L-E	3	84	0.26	0.44	0.30	0.00	0.00	0.00	0.00
1-3A	4	102	0.31	0.00	0.25	0.00	0.00	0.00	0.44
1-3B	4	53	0.49	0.04	0.47	0.00	0.00	0.00	0.00
1-3C	4	29	0.24	0.10	0.48	0.17	0.00	0.00	0.00
1-3D	4	42	0.29	0.02	0.60	0.02	0.00	0.00	0.07
1-4C	5	59	0.41	0.00	0.51	0.05	0.00	0.00	0.03
1-4D	5	44	0.16	0.05	0.70	0.07	0.00	0.00	0.02
1-5A	6	46	0.54	0.00	0.30	0.00	0.00	0.00	0.15
1-8A	8	99	0.76	0.01	0.23	0.00	0.00	0.00	0.00
1-8B	8	19	0.11	0.11	0.63	0.16	0.00	0.00	0.00
1-9B	9	94	0.09	0.17	0.48	0.12	0.04	0.00	0.11
1-9C	9	118	0.16	0.17	0.35	0.29	0.00	0.00	0.03
1-9D	9	117	0.33	0.13	0.27	0.18	0.01	0.00	0.08
1-9E	9	88	0.07	0.26	0.26	0.24	0.00	0.00	0.17
1-9L-A	9	60	0.25	0.08	0.37	0.15	0.12	0.00	0.03
1-9L-B Sq	9	124	0.27	0.08	0.51	0.09	0.03	0.00	0.02
1-9L-B Long	9	111	0.44	0.04	0.37	0.10	0.00	0.01	0.05
1-9L-C	9	119	0.45	0.03	0.29	0.09	0.06	0.03	0.04
1-9L-D	9	106	0.24	0.09	0.44	0.14	0.01	0.06	0.02
1-9L-E	9	71	0.17	0.17	0.28	0.32	0.00	0.00	0.06
1-10A	10	135	0.30	0.05	0.36	0.04	0.18	0.04	0.03
1-10B	10	104	0.49	0.05	0.38	0.08	0.01	0.00	0.00
1-10C	10	100	0.35	0.00	0.23	0.00	0.38	0.04	0.00
1-10D	10	149	0.32	0.05	0.32	0.10	0.18	0.00	0.03
1-10E	10	202	0.37	0.00	0.46	0.04	0.10	0.01	0.01
avg.			0.30 (0.14)	0.09 (0.09)	0.40 (0.13)	0.11 (0.09)	0.03 (0.08)	0.01 (0.01)	0.06 (0.09)

Table 6: Number of vesicles classified and proportions of each vesicle type in Mt. Pinatubo dense cognate lithics.

surge event	n. vesicles	smooth spherical	rough spherical	smooth ellipzoidal	rough ellipzoidal	sharp-tipped ellipzoidal	stretched distorted	distorted	rough spherical + rough ellipzoidal
1	373	20.91	9.65	46.38	11.80	1.34	0.27	9.65	21.45
3	725	29.38	13.10	38.21	11.45	0.00	0.14	7.72	24.55
4	226	34.07	2.65	39.38	2.65	0.00	0.00	21.24	5.31
5	103	30.10	1.94	59.22	5.83	0.00	0.00	2.91	7.77
6	46	54.35	0.00	30.43	0.00	0.00	0.00	15.22	0.00
8	118	65.25	2.54	29.66	2.54	0.00	0.00	0.00	5.08
9	1008	25.89	11.81	36.61	16.57	2.38	0.99	5.75	28.37
10	690	35.94	2.90	36.38	5.22	16.09	1.74	1.74	8.12

Table 7: Proportions of vesicles of each vesicle type in Mt. Pinatubo pre-climactic dense cognate lithics based on surges.

sample	hiatus time	accumulated time	avg. H_2O (wt.%)	max. H_2O (wt.%)	min. H_2O (wt.%)	H_2O range (wt.%)	avg. CO_2 (ppm)	CO_2 range (ppm)
3-6D	124	124	1.302	1.44	1.01	0.43	9	3
1-2A	262	386	1.881	2.13	1.52	0.61	25	14
1-2B	262	386	1.283	1.45	0.71	0.74	18	18
1-2C	262	386	1.833	2.11	1.54	0.57	28	12
1-2L-A	262	386	1.620	1.78	1.42	0.36	22	14
1-2L-B	262	386	1.302	1.44	1.01	0.43	19	17
1-2L-C	262	386	1.550	1.72	0.87	0.85	22	10
1-2L-E	262	386	1.647	2.1	1.2	0.9	21	18
1-3A	112	498	1.791	2.09	1.41	0.68	18	15
1-3B	112	498	1.718	1.92	1.52	0.40	15	12
1-3C	112	498	1.642	1.72	1.59	0.13	21	12
1-3D	112	498	1.981	2.37	1.51	0.86	18	10
1-4B	90	588	1.627	1.91	1.22	0.69	15	10
1-4C	90	588	1.868	2.04	1.76	0.28	15	10
1-4D	90	588	1.960	2.15	1.68	0.47	20	15
1-5A	174	762	1.547	2.00	1.32	0.68	20	14
1-8B	137	1031	1.673	2.58	1.46	1.12	23	13
1-8C	137	1031	1.649	2.58	1.42	1.16	10	10
1-8D	137	1031	1.814	1.87	1.76	0.10	19	3
1-8E	137	1031	1.383	1.83	1.21	0.62	8	8
1-9B	46	1072	1.075	1.13	1.02	0.11		
1-9C	46	1072	1.290	1.53	1.12	0.41	10	8
1-9D	46	1072	1.568	2.35	1.09	1.26	9	3
1-9E	46	1072	1.788	2.28	1.15	1.13	11	
1-9L-A	46	1072	1.482	1.8	1.22	0.58	8	7
1-9L-B (sq)								15
1-9L-B (long)	46	1072	1.449	1.58	1.22	0.36	16	10
1-9L-C Part 1	46	1072	1.444	1.6	1	0.6	5	3
1-9L-C Part 2	46	1072	1.526	2.05	0.82	1.23	9	5
1-9L-D	46	1072	1.312	1.65	1.04	0.61	9	2
1-10A	33	1105	1.363	1.81	1.13	0.68	7	1
1-10B	33	1105	1.137	1.56	0.62	0.94	7	4
1-10C	33	1105	1.297	1.41	1.15	0.26	5	2
1-10D	33	1106	1.598	2.05	1.35	0.7	8	3

1-10E	33	1105	1.583	2.18	1.18	1	6	3

Table 8: Dissolved H_2O and CO_2 concentrations measured in matrix glass of 1991 Mt. Pinatubo pre-climactic dense cognate lithics.

surge	sample	SiO_2 (wt.%)	TiO_2 (wt.%)	Al_2O_3 (wt.%)	FeO (wt.%)	MnO (wt.%)	MgO (wt.%)	CaO (wt.%)	Na_2O (wt.%)	K_2O (wt.%)	sum (wt.%)
1	1-1B	78.81	0.07	12.39	0.73	0.01	0.16	0.92	3.71	3.21	100.00
1	1-1B	78.45	0.10	12.13	0.87	0.05	0.19	1.04	4.11	3.06	100.00
1	1-1B	77.99	0.13	12.54	0.73	0.02	0.24	1.17	4.06	3.12	100.00
1	1-1B	77.66	0.13	12.40	0.97	0.03	0.38	1.24	4.13	3.07	100.00
1	1-1B	78.25	0.11	12.26	0.86	0.03	0.18	1.14	3.99	3.18	100.00
1	1-1B	77.87	0.15	12.43	0.86	0.02	0.15	1.14	4.24	3.14	100.00
Avg. (Std dev.)		78.17 (0.42)	0.12 (0.03)	12.36 (0.14)	0.84 (0.09)	0.03 (0.01)	0.22 (0.08)	1.11 (0.11)	4.04 (0.18)	3.13 (0.06)	
3	1-2B	79.01	0.10	11.81	1.01	0.01	0.13	1.04	3.68	3.21	100.00
3	1-2B	78.73	0.16	12.04	0.87	0.06	0.16	0.98	3.71	3.27	100.00
3	1-2B	78.64	0.13	12.32	0.78	0.06	0.19	1.03	3.57	3.29	100.00
3	1-2B	78.93	0.10	12.07	0.76	0.05	0.20	0.94	3.70	3.25	100.00
3	1-2B	78.65	0.14	12.21	0.75	0.05	0.16	0.98	3.77	3.29	100.00
3	1-2B	78.45	0.23	12.38	1.04	0.02	0.15	1.06	3.47	3.21	100.00
3	1-2B	79.01	0.16	12.20	0.69	0.04	0.19	1.09	3.35	3.27	100.00
Avg. (Std dev.)		78.77 (0.21)	0.15 (0.05)	12.15 (0.19)	0.84 (0.14)	0.04 (0.02)	0.17 (0.03)	1.02 (0.05)	3.61 (0.15)	3.25 (0.03)	
4	1-3B	78.87	0.09	12.37	0.76	0.03	0.17	1.01	3.49	3.22	100.00
4	1-3B	78.78	0.08	12.28	0.71	0.01	0.16	1.05	3.85	3.08	100.00
4	1-3B	78.61	0.11	12.25	0.75	0.03	0.19	1.00	3.63	3.42	100.00
4	1-3B	78.47	0.15	12.61	0.85	0.04	0.26	1.14	3.30	3.17	100.00
4	1-3B	78.88	0.16	12.29	0.76	0.00	0.22	0.98	3.57	3.14	100.00
4	1-3B	78.31	0.15	12.54	0.64	0.05	0.20	1.08	3.80	3.22	100.00
4	1-3B	78.58	0.15	12.42	0.76	0.03	0.14	1.04	3.72	3.16	100.00
4	1-3B	78.95	0.12	12.15	0.79	0.04	0.20	0.95	3.62	3.19	100.00
4	1-3B	78.37	0.10	12.66	0.70	0.00	0.11	1.16	3.97	2.94	100.00
4	1-3B	78.99	0.17	12.42	0.82	0.03	0.16	1.02	3.32	3.06	100.00
4	1-3B	78.47	0.10	12.40	0.68	0.03	0.17	1.06	3.92	3.18	100.00
Avg. (Std dev.)		78.66 (0.24)	0.13 (0.03)	12.40 (0.16)	0.75 (0.06)	0.03 (0.02)	0.18 (0.04)	1.04 (0.06)	3.65 (0.22)	3.16 (0.12)	
5	1-4B	78.37	0.18	12.52	0.67	0.03	0.14	1.11	3.79	3.17	100.00
5	1-4B	78.43	0.11	12.50	0.70	0.02	0.15	1.05	3.94	3.09	100.00
5	1-4B	78.30	0.14	12.46	0.70	0.02	0.16	1.06	3.97	3.17	100.00
5	1-4B	78.31	0.08	12.69	0.71	0.07	0.18	1.01	3.96	2.98	100.00
5	1-4B	78.02	0.15	12.75	0.83	0.00	0.14	1.04	3.97	3.10	100.00
5	1-4B	78.54	0.09	12.51	0.72	0.00	0.23	1.04	3.88	2.99	100.00
5	1-4B	78.53	0.14	12.36	0.73	0.07	0.21	1.03	3.76	3.16	100.00
5	1-4B	78.48	0.09	12.59	0.74	0.02	0.18	1.07	3.78	3.07	100.00
Avg. (Std dev.)		78.37 (0.17)	0.12 (0.04)	12.55 (0.13)	0.73 (0.05)	0.03 (0.03)	0.18 (0.03)	1.05 (0.03)	3.88 (0.09)	3.09 (0.08)	
6	1-5A	79.01	0.12	12.20	0.71	0.02	0.11	1.05	3.78	2.99	100.00
6	1-5A	77.80	0.14	12.90	0.65	0.09	0.10	1.27	4.22	2.83	100.00
6	1-5A	77.43	0.14	12.89	0.73	0.06	0.10	1.28	4.33	3.03	100.00
6	1-5A	77.37	0.16	13.16	0.71	0.04	0.13	1.23	4.00	3.19	100.00
6	1-5A	77.84	0.07	13.18	0.66	0.03	0.07	1.25	4.03	2.88	100.00
6	1-5A	78.32	0.14	12.32	0.76	0.06	0.14	1.07	3.94	3.23	100.00
Avg. (Std dev.)		77.96 (0.62)	0.13 (0.03)	12.78 (0.42)	0.71 (0.04)	0.05 (0.03)	0.11 (0.03)	1.19 (0.10)	4.05 (0.20)	3.03 (0.16)	
8	1-8C	78.51	0.14	12.48	0.78	0.00	0.19	1.05	3.80	3.04	100.00
8	1-8C	77.99	0.11	12.66	0.82	0.03	0.16	1.06	4.11	3.06	100.00
8	1-8C	78.10	0.14	12.56	0.98	0.00	0.19	1.07	3.84	3.11	100.00
8	1-8C	78.31	0.14	12.49	0.78	0.04	0.18	1.09	3.93	3.03	100.00
8	1-8C	78.03	0.13	12.54	0.77	0.01	0.23	1.17	4.02	3.11	100.00
8	1-8C	77.95	0.17	12.69	0.71	0.06	0.22	1.09	4.09	3.03	100.00
8	1-8C	77.65	0.17	12.65	0.90	0.07	0.18	1.07	4.09	3.22	100.00
8	1-8C	78.10	0.17	12.51	0.87	0.05	0.17	1.02	4.09	3.02	100.00

Avg. (Std dev.)		78.08 (0.26)	0.15 (0.02)	12.57 (0.08)	0.82 (0.09)	0.03 (0.03)	0.19 (0.02)	1.08 (0.04)	4.00 (0.13)	3.08 (0.07)	
9	1-9D	77.61	0.14	12.70	0.77	0.08	0.30	1.15	4.16	3.09	100.00
9	1-9D	77.44	0.11	12.79	0.88	0.04	0.20	1.17	4.27	3.10	100.00
9	1-9D	77.42	0.14	12.75	0.79	0.02	0.18	1.15	4.46	3.10	100.00
9	1-9D	77.90	0.10	12.71	0.75	0.04	0.24	1.19	4.03	3.04	100.00
9	1-9D	77.94	0.15	12.86	0.69	0.00	0.17	1.15	4.01	3.03	100.00
9	1-9D	78.18	0.13	12.69	0.75	0.02	0.22	1.09	3.77	3.16	100.00
9	1-9D	77.81	0.09	12.54	0.85	0.01	0.22	1.17	4.15	3.16	100.00
Avg. (Std dev.)		77.76 (0.28)	0.12 (0.02)	12.72 (0.10)	0.78 (0.07)	0.03 (0.03)	0.22 (0.05)	1.15 (0.03)	4.12 (0.22)	3.10 (0.05)	
10	1-10B	77.56	0.13	12.89	0.75	0.05	0.21	1.19	4.12	3.10	100.00
10	1-10B	77.52	0.13	12.71	0.79	0.04	0.26	1.16	4.27	3.13	100.00
10	1-10B	78.02	0.06	12.61	0.78	0.01	0.22	1.18	4.06	3.06	100.00
10	1-10B	77.80	0.14	12.62	0.83	0.05	0.22	1.14	3.99	3.20	100.00
10	1-10B	77.55	0.11	12.77	0.80	0.02	0.18	1.17	4.18	3.23	100.00
10	1-10B	78.58	0.13	12.27	0.78	0.04	0.22	1.19	3.76	3.01	100.00
10	1-10B	77.65	0.10	12.66	0.86	0.07	0.26	1.31	3.94	3.14	100.00
Avg. (Std dev.)		77.81 (0.38)	0.11 (0.03)	12.65 (0.19)	0.80 (0.04)	0.04 (0.02)	0.23 (0.03)	1.19 (0.06)	4.04 (0.17)	3.13 (0.08)	

Table 9: Matrix glass composition (in brackets are 1 σ of oxide concentration measurements).

References

Bernard A, Knittel U, Weber B, Weis D, Albrecht A, Hattori K, Oles D (1996) Petrology and geochemistry of the 1991 eruption products of Mount Pinatubo. Fire and mud: eruptions and lahars of Mount Pinatubo, Philippines, 767-797

Bursik M (1993) Subplinian eruption mechanisms inferred from volatile and clast dispersal data. J Volcanol Geotherm Res 57:57–70

Eichelberger JC, Carrigan CR, Westrich HR, Price RH (1986) Non-explosive silicic volcanism. Nature, 323(6089), 598

Eichelberger JC, Westrich HR (1981) Magmatic volatiles in explosive rhyolitic eruptions. Geophysical research letters, 8(7), 757-760

Gardner JE, Llewellin EW, Watkins JM, Befus KS (2017) Formation of obsidian pyroclasts by sintering of ash particles in the volcanic conduit. Earth Planet Sci Lett 459:252–263

Gardner JE, Wadsworth FB, Llewellin EW, Watkins JM, Coumans JP (2018) Experimental sintering of ash at conduit conditions and implications for the longevity of tuffisites. Bull Volcanol 80:23

Gardner JE, Wadsworth FB, Llewellin EW, Watkins JM, Coumans JP (2019) Experimental constraints on the textures and origin of obsidian pyroclasts. Bull Volcanol, 81(4): 22

Gonnermann HM, Manga M (2005a) Nonequilibrium magma degassing: results frommodeling of the ca. 1340 AD eruption of Mono Craters, California. Earth Planet Sci Lett 238(1):1–16

Gonnermann HM, Manga M (2005b) Flow banding in obsidian: a record of evolving textural heterogeneity during magma deformation. Earth Planet Sci Lett 236(1):135–147

Hammer JE, Cashman KV, Hoblitt RP, Newman S (1999) Degassing and microlite crystallization during pre-climactic events of the 1991 eruption of Mt. Pinatubo, Philippines. Bull Volcanal, 60(5): 355-380

Hildreth W, Drake RE (1992) Volcan Quizapu, Chilean Andes. Bull Volcanol 54: 93–125

Hoblitt RP, Wolfe EW, Scott WE, Couchman MR, Pallister JS, Javier D (1996) The Preclimactic Eruptions of Mount Pinatubo, June 1991. Fire and Mud: eruptions and lahars of Mount Pinatubo, Philippines, 457-511

Jaupart C, Allegre CJ (1991) Gas content, eruption rate and instabilities of eruption regime in silicic volcanoes. Earth Planet Sci Lett 102:413–429

Liu Y, Zhang Y, Behrens H (2005) Solubility of H_2O in rhyolitic melts at low pressure and a new empirical model for mixed H_2O-CO_2 solubility in rhyolitic melts. J Volcanol Geotherm Res 143:219–235

Luhr JF, Melson WG (1996) Mineral and glass compositions in June 15, 1991, pumices: evidence for dynamic disequilibrium in the dacite of Mount Pinatubo. Fire and Mud: Eruptions and Lahars of Mount Pinatubo, Philippines, 733-750

Martel C, Iacono-Marziano G (2015) Timescales of bubble coalescence, outgassing, and foam collapse in decompressed rhyolitic melts. Earth Planet Sci Lett 412:173-185

Mastrolorenzo G, Munno R, Rolandi G (1993) Vesuvius 1906; a case study of a paroxysmal eruption and its relation to eruption cycles. J Volcanol Geotherm Res 58 :217–237

Mellors RA, Sparks RSJ (1991) Spatter-rich pyroclasitc flow deposits on Santorini, Greece. Bull Volcanol 53 :327–342

Newman S, Epstein S, Stolper E (1988) Water, carbon dioxide and hydrogen isotopes in glasses from the ca. 1340 A.D. eruption of the Mono Craters, California: constraints on degassing phenomena and initial volatile content. J Volcanol Geotherm Res 35:75–96

Pallister JS, Hoblitt RP, Meeker GP, Knight RJ, Siems DF (1996). Magma mixing at Mount Pinatubo: petrographic and chemical evidence from the 1991 deposits. Fire and mud: eruptions and lahars of Mount Pinatubo, Philippines, 687-731

Rust AC, Cashman KV (2007) Multiple origins of obsidian pyroclasts and implications for changes in the dynamics of the 1300 B.P. eruption of Newberry Volcano, USA. Bull Volcanol 69:825–845

Rust AC, Cashman KV, Wallace PJ (2004) Magma degassing buffered by vapor flow through brecciated conduit margins. Geology 32:349–352

Rust AC, Manga M (2002). Bubble shapes and orientations in low Re simple shear flow. J. Colloid Interface Sci 249: 476–480

Rutherford MJ, Devine JD (1996) Preeruption pressure-temperature conditions and volatiles in the 1991 dacitic magma of Mount Pinatubo. Fire and mud: eruptions and lahars of Mount Pinatubo, Philippines, 751-766

Scott WE, Hoblitt RP, Torres RC, Self S, Martinez ML, Nillos T Jr (1996) Pyroclastic Flows of the June 15, 1991, Climactic Eruption of Mount Pinatubo. Fire and mud: eruptions and lahars of Mount Pinatubo, Philippines, 545-570

Swanson SE (1977) Relation of nucleation and crystal-growth rate to the development of granitic textures. Am Mineral 62:966–978

Taylor GI (1934) The formation of emulsions in definable fields of flow. Proc. R. Soc. Lond. Ser A146: 501–523

Taylor BE, Eichelberger JC, Westrich HR (1983) Hydrogen isotopic evidence of rhyolitic magma degassing during shallow intrusion and eruption. Nature 306:541–545

Wolfe EW, Hoblitt RP (1996) Overview of the eruptions. Fire and Mud: eruptions and lahars of Mount Pinatubo, Philippines, 3-20

Wright TL, Doherty PC (1970) A linear programming and least squares computer method for solving petrologic mixing problems. Geological Society of America Bulletin, 81(7), 1995-2008

Zhang Y, Belcher R, Ihinger PD, Wang L, Xu Z, Newman S (1997) New calibration of infrared measurement of dissolved water in rhyolitic glasses. Geochim Cosmochim Acta 61:3089–3100